Feasibility of Nuclear Plasma Interaction studies with the Activation Technique

Thembalethu Nogwanya

A thesis submitted in partial fulfillment for the
of Master of Science in the Department of Physics and Astronomy,

UNIVERSITY OF THE WESTERN CAPE

Supervisor: Dr Mathis Wiedeking (iThemba LABS)
Co-Supervisors: Dr D.L. Bleuel (Lawrence Livermore National Laboratory)
Prof J.N. Orce (University of the Western Cape)

28th August 2018

Declaration of Authorship

I declare that this thesis titled, *"Feasibility of Nuclear Plasma Interaction studies with the Activation Technique"* is my own work, that it has not been submitted for any degree or examination in any other university, and that all the sources I have used or quoted have been indicated and acknowledged by complete references.

Full name: Thembalethu Nogwanya

Signed:

Date: 28th August 2018

i

"It is a law of life that problems arise when conditions are there for their solution."

Walter Sisulu

Keywords

'Feasibility of Nuclear Plasma Interaction studies with the Activation Technique'

Thembalethu Nogwanya

IC

BIC

EC

NPI's

HEDP's

DIGS

NEEC

NEET

Plasma

S-process

R-process

P-type detector

N-type detector

Abstract

Feasibility of Nuclear Plasma Interaction studies with the Activation Technique

Thembalethu Nogwanya

Master of Science Degree

Electron-mediated nuclear plasma interactions (NPIs), such as Nuclear Excitation by Electron Capture (NEEC) or Transition (NEET), can have a significant impact on nuclear cross sections in High Energy Density Plasmas (HEDPs). HEDP environments are found in nuclear weapons tests, National Ignition Facility (NIF) shots and in the cosmos where nucleosynthesis takes place. This thesis explores the impact of NPIs on highly excited nuclei. This impact is understood to be more intense in highly-excited nuclei states in the quasi-contiuum which is populated by nuclear reactions prior to their decay by spontaneous γ-ray emission. Attempts thus far have failed in measuring the NEEC process [1, 2], while NEET process has been observed experimentally [3, 4]. Direct observation of NPIs is hindered by the lack of a clear signature of their effect in HEDP environments. Hence this should test a new signature [5] for NPIs for highly-excited nuclei by investigating isomeric to ground state feeding from the isomeric state. An experiment was performed using the reactions ^{197}Au(^{13}C, ^{12}C)^{198}Au and ^{197}Au(^{13}C, ^{12}C2n)^{196}Au at Lawrence Berkeley National Laboratory in inverse kinematics with an ^{197}Au beam of 8.5 MeV/u energy. Several measurements were performed with different target configurations. The activated foils were counted at the low-background counting facility of Lawrence Livermore National Laboratory. From these data, the double isomeric to ground state ratio (DIGS) were extracted with the assistance of the decay equations that were included in the experiment. As the NPIs effects are rather small the lines for analysis had to be chosen carefully so that the extracted ratios would not contain significant errors. The measured DIGS ratios were then compared with the result of the theoretical DIGS ratios. The results showed that the calculated DIGS ratios deviated substantially from unity although this was with large uncertainties. Because of the large errors obtained, the DIGS ratios were found to be inconclusive as a signature for detecting the effects of NPIs such as angular momentum distribution changes in HEDP environments.

Acknowledgements

Contents

I would like to dedicate this work to my dear father S. Nogwanya

`(Mvulane, Msuthu, Ncilashe, Bhayi, Khetsha...)`

And to my dear mother N.B. Nogwanya for their unconditional love and wanting me to be myself `(Xhamela, Nokwindla, Thyopho ka Phato, Helushe, Ncancashe...)`

To my dear sister N. Nogwanya and my young brother Y. Nogwanya and lastly to all my entire family.

Thembalethu Nogwanya

Chapter 1

Introduction

Over the last decades, the processes of electron nuclei-plasma interactions have been studied extensively theoretically and experimentally. Nuclear plasma interactions (NPIs) such as Nuclear Excitation by Electron Capture (NEEC) or Transition (NEET) are rare nuclear excitations that are theorized to occur in certain isotopes [6]. NEET and NEEC are expected to cause significant changes in reaction cross sections in High Energy Density Plasmas (HEDPs) such as those found in the National Ignition facility (NIF) shots and astrophysical settings [7]. For NEEC, a free electron is resonantly captured into a bound atomic state and the same time it transfers its capture energy to the nucleus, which undergoes a transition from the ground state to an excited state. For the NEET process, atomic electrons transition with binding energy difference equal to the nuclear excitation energy. Then, for NEET, the binding energy and, for NEEC, the free electron energy plus the binding energy is resonantly transferred to the nucleus via a virtual photon and the nucleus becomes excited. In the end, whether we talk of the NEEC or NEET process, NPIs remain hardly accessible via many experiments because of the extreme narrowness of nuclear transitions ($\Gamma \leq 1$ μeV).

1.1 Astrophysical Environments

For a star in thermal equilibrium, an internal energy source is required to balance the energy that is lost in the form of radiation from its surface. This energy source is provided by nuclear reactions that take place in the interior of the star, where the temperatures and densities are very high temperatures $T \simeq 200$ MeV [8]. Apart from the energy generation nuclear reactions that take place in stars can

1

change the stars composition through transmutation of one element into another. Thus, an understanding of NEEC and NEET may play a major role in production or destruction of isotopes since isotopes evolution undergoes several processes.

In the context of nucleosynthesis, the formation of the heavier elements comes from the absorption of neutrons and protons by the pre-existing nuclei [9]. The absorption of a neutron is sometimes slow and the formed nuclei usually beta decay back to the beta-stability curve before absorbing the next neutron. This process is known as the slow neutron capture (S-process) [10]. Though, if the neutron flux is very high, the nuclei will capture as many neutrons as it can which tend to be too fast for beta decay to occur and can be driven to extremely neutron-rich nuclei. This process may happen during explosive scenarios, for example, core-collapse supernovae and neutron star mergers where there are high neutron densities and temperatures and this rapid creation is called (R-process) [11].

1.2 NEEC and NEET in plasma environment

In this work, we are mainly concerned with the role of the NEEC and NEET process in the cosmogenic nucleosynthesis. In the internal conversion (IC) process, the energy released from the nucleus is used to expel an orbital electron (bound state) from the atom to the continuum. Bound internal conversion (BIC) is the same as the IC but here the electron is promoted to the bound state and electron capture (EC) is the type of decay in which the nucleus of an atom draws in an inner shell electron. Hence NEEC and NEET could play a major role in the formation of heavier elements since both these process are time inverses of IC, BIC, and EC. These processes are expected to allow determination of atomic vacancy effects on nuclear lifetimes and population mechanisms of excited nuclear levels through an influx of electrons [12].

1.3 Motivation and study objectives

The electron-mediated nuclear plasma environment can enhance the population of nuclear-excited states through the coupling of nuclear transitions to transitions including bound atomic states of the charged ions. The processes that can occur,

nuclear excitation by electron transition (NEET) and nuclear excitation by electron capture (NEEC), are difficult to calculate owing to the many-body physics of the atomic system and plasma consequences on atomic level widths and densities.

There have been broad theoretical studies that have been undertaken to try to study these two processes [13–15]. Amongst these, attempts to measures NEEC have been unsuccessful [16], including attempts to detect the NEEC process resonantly by exciting the ground state of ^{181}Ta and ^{187}Os in plasmas generated by the Omega Facility at the Laboratory for Laser Energetics at the University of Rochester [17].

The limited observations of the parallel bound-state process NEET are controversial and have been restricted to non-plasma environments [18–20]. This study attempts to fill in those gapes by inducing NPIs in highly-excited nuclear states produced by nuclear reactions prior to their decay by spontaneous γ-ray emissions. The large density of nuclear states at these high excitation energies increases the probability that the energy from the atomic transition will resonantly match an available nuclear transition. To this end we observe the NPI effects following the $(n, 2n)$ reaction at the National Ignition Facility (NIF), which populates states several MeV below the neutron separation energy prior to γ-ray emission. Despite the fact that energy transfer by NPIs is small, changes in angular momentum are likely to occur even with this small energy transfer in highly-excited nuclei.

A new experimental approach to detect the signature of NPIs on highly-excited nuclei was proposed by D. L. Bleuel et. al., [5]. This novel experimental method is called "the differential population of high-spin isomeric versus the ground state of the de-excited nucleus". In particular the ^{134}Xe$(n, 2n)$ reaction was proposed, which has a long-lived ($t_{\frac{1}{2}} = 2.2$-days) $11/2^-$isomer and a ($t_{\frac{1}{2}} = 5.2$-days) $3/2^+$ ground state. The effect of NPIs of producing differential isomer population for reaction products exposed to a plasma or non-plasma environment is discussed in detail in Section 3.5 (also see Figure 3.9). The Double-Isomer-to-Ground-State (DIGS) ratio for the ^{133m}Xe / ^{133}Xe fraction formed in the exploding pusher capsule plasma divided by the same quantity for an externally-mounted, non-plasma Target option Activation Device (TOAD) sample, illustrates whether NPIs had effect on highly-excited states in ^{133}Xe. The DIGS ratio is given by:

$$R_{DIGS} = \frac{N^{Xe-133m}_{capsule}/N^{Xe-133}_{capsule}}{N^{Xe-133m}_{TOAD}/N^{Xe-133}_{TOAD}} \qquad (1.1)$$

with N being the number of each state populated, determined from its characteristic-energy γ-ray emissions measured in a high-purity germanium detector.

The primary goal of this thesis is to calculate the DIGS ratio on highly excited states using the activation technique and the ^{197}Au(^{13}C, ^{12}C)^{198}Au and ^{197}Au(^{13}C, ^{12}C2n)^{196}Au reactions at Lawrence Berkeley National Laboratory in inverse kinematics with a ^{197}Au beam of 8.5 $MeV/$u energy. These Au isotopes have similarly long-lived 12^- isomers and 2^- ground states compared to Xe.

The γ-ray decays from the isomer and ground state will be measured following the activation in a simulated plasma and non-plasma environments. The plasma environments will be simulated by using different target configurations (see Section 3.3 the targets illustration on the following Figures 3.5, 3.6 and 3.7). From the decay data differences in the feeding of the isomer versus ground state (the proposed signature for NPI) will be investigated. If angular momentum is changed due to NPIs the feeding pattern may different. This change in feeding is at the lane of this thesis to investigate if the proposed method is feasible to detect NEEC or NEET.

Chapter 2

Interaction of γ ray with matter

2.1 Types of interaction with matter

When charged particles, photons, and neutral particles penetrate a material some
of the energy from the particles may be absorbed completely, some may be scat-
tered and some may pass through without any interactions with the material.
The process of absorption, scattering and pair production can be described and
explained in terms of interaction between particles. There are different kinds of
interaction through which a particle passing through a material can deposit its
energy. In this chapter, we consider the interaction of photons with matter.

2.1.1 Attenuation

As a photon passes through matter, there is no way to precisely know how far it
will take before being involved in an interaction or what type of interaction it will
be involved in. Either Compton or photoelectric interactions will absorb some of
the photons from the beam of particles. This process is known as attenuation [21].
Suppose at some distance, x, into the material N_0 photons are moving through
a slab of material. Then after exiting the material the number of photons in the
beam is reduced. The following Equation 2.1 shows how the number of photons is
reduced [21],

$$N_x = N_0 e^{-\mu x}, \tag{2.1}$$

5

where μ is known as the linear attenuation coefficient and is the actual fraction of photons interacting per unit thickness of the material. The exponential decay in Equation 2.1 comes from the fact that over a short distance, the probability of losing a particle from the beam is proportional to the number of particles left (see Figure 2.1).
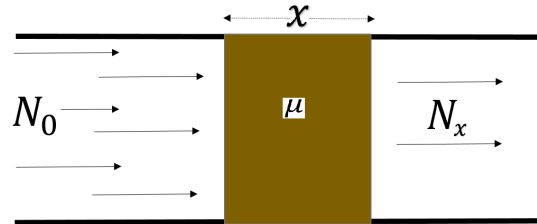
Figure 2.1 – A schematic of a linear attenuation, N_0 is the number of incoming photons and N_x is the number of photons after passing the slab.

2.1.2   Photoelectric effect

In the process of the photoelectric effect, a photon gets absorbed by the atomic electron which is then ejected from the atom. This only happens if the incoming photon energy is larger than the electron binding energy. Because the atom is much heavier when compared to the mass of an electron, the ejected electron will practically take all the energy and momentum of the incoming photon (see Figure 2.2). The kinetic energy of the ejected electron, E_K, is then given by:

$$E_K = hf - E_B, \tag{2.2}$$

where h is the Planck constant which is equal to $6.62607004 10^{-34} m^2 kg/s$, f is the frequency of the incident photon and E_B is the electron binding energy. The ejected electron is known as the photoelectron.

The probability of photoelectric absorption depends on the photon energy, the binding energy of the electron and the atomic number of the atom, Z. The probability of this process increases the more bound the electron is to the nucleus. Hence K-shell electrons are the most affected ones provided that γ-ray energy exceeds the K-electron binding energy. The probability for this is given by the following relation [22]:
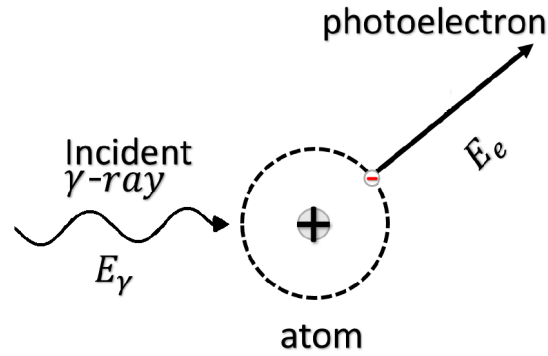
Figure 2.2 – A schematic of the photoelectric absorption.

$$\mu_m \propto Z^4/E_\gamma^3, \tag{2.3}$$

where μ_m is the photoelectric mass attenuation coefficient which is the rate of photon interactions per 1-unit (g/cm^2) area mass and Z is the atomic number of the atom. Figure 2.3 shows how the attenuation varies with photon energy. The decrease of μ_m with the increase in energy is interrupted by a series of jumps, called absorption edges.
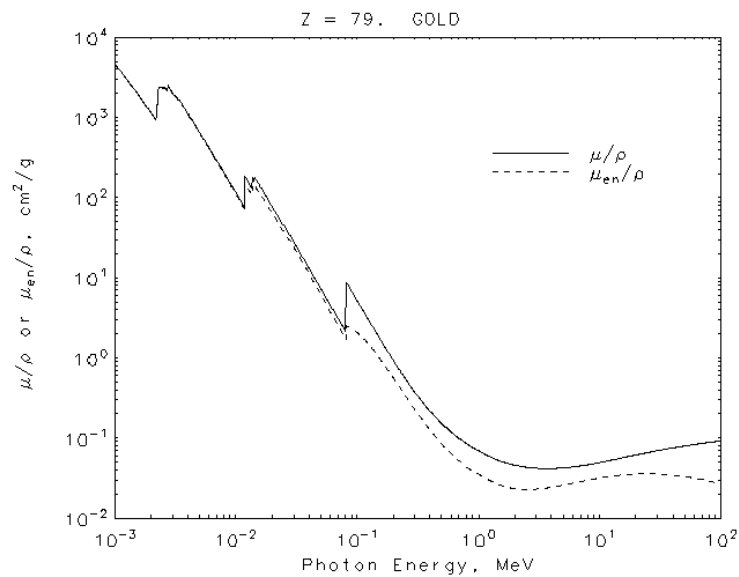
Figure 2.3 – A schematic of the mass attenuation for Au = 79, μ_m/ρ and the mass energy-absorption coefficient μ_{en}/ρ as the function of photon energy [23].

The probability of the photoelectric absorption increases as the photon energy decreases. It also becomes smaller after the absorption edge. This is because the photon energy does not have enough energy to remove the electron in the atomic

shell, as seen in Figure 2.3. The determination of the mass attenuation coefficient for gold was carried out by J. L. Glover et al., [24].

2.1.3 Compton scattering

In Compton scattering, the γ ray directly interacts with a free or a bound electron. After the interaction, the γ ray scatters, see Figure 2.4. The recoil energy of the electron is equal to the difference of the energy lost by the γ ray and the electron binding energy (Equation 2.4).
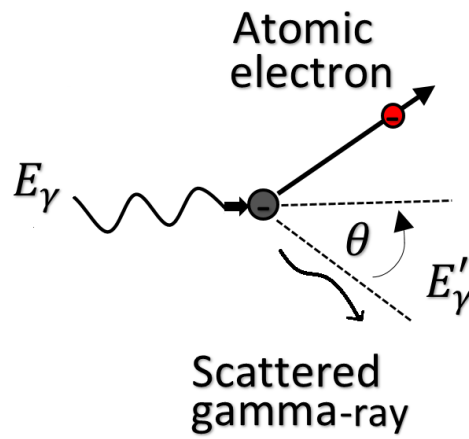
Figure 2.4 – A schematic diagram of Compton scattering.

The law of conservation of mass-energy and conservation of momentum limits the maximum kinetic energy of the photoelectron. The value for the scattered photon energy is given by the following relation [22]:

$$E_{\gamma}^{'} = \frac{M_0 c^2}{(1 - cos(\theta) + \frac{M_0 c^2}{E_{\gamma}})}, \qquad (2.4)$$

where $M_0 c^2$ is the electron rest mass energy of 511 keV, and θ is the angle between the incident and scattered photon shown in Figure 2.4. The direction of the electron and the γ ray is dependent on the γ-ray energy which is transferred to the electron. When Compton scattering takes place in a detector, the scattered electron is usually stopped in the detection medium. The detector gives an output pulse that is proportional to the lost energy of the incident γ ray. This energy depends on the scattering angle, θ, [21]. As shown in Figure 2.5 the probability of Compton scattering becomes small as the energy of the γ ray become larger.

Furthermore, Compton scattering is weakly dependent on the atomic number, of the absorbing material.

2.1.4 Pair production

In general pair production is an event where γ-ray energy is directly converted to matter. For pair production to happen the γ ray must have an energy of at least 1.022 MeV (mass of two electrons). With the interaction of the electromagnetic field of the nucleus of an atom the energy is converted into the mass of an electron-positron pair. The γ ray disappears as an electron-positron pair appears. The positron that is formed quickly disappears by reconversion into photons in the process of annihilation with another electron in matter. The annihilation converts the rest masses of the electron and positron into two 0.511 MeV γ rays, emitted in opposite directions (see Figure 2.6).
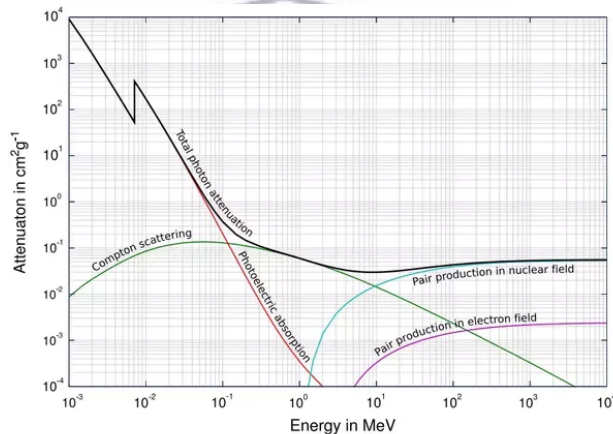
Figure 2.5 – The linear absorption coefficient for Compton scattering, photoelectric effect, pair production and total photon attenuation [25]. This figure represents photon interaction the vertical axis represent the mass attenuation coefficient, which is discussed in Section 2.1.1.

It can be seen in Figure 2.5, for low photon energy, the photoelectric effect is the predominant process, with Compton scattering happening over all energies but peaks in the midrange, while pair production occurs only above 1.022 MeV and dominates as the photon energy increases.
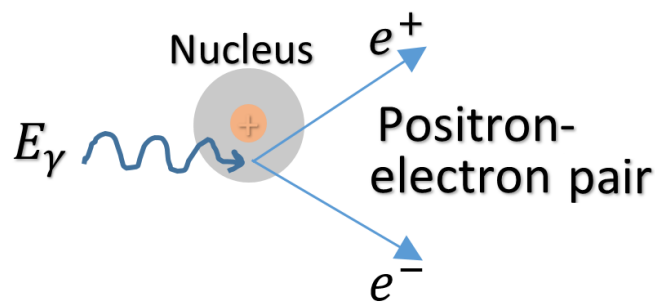
Figure 2.6 – A schematic diagram of pair production

2.2   Germanium Detector

Germanium semiconductor detectors are commonly used to detect γ rays that are
emitted in the nuclear process during radioactive decay. The γ-ray photons will
give some or all the energy to an electron in the material. The ionized atom will
then further collide with other electrons and result in many more electrons being
created. A germanium detector is an intrinsic semiconductor, and the presence
of any donor such as lithium or acceptor such as boron impurities will cause
the material to be either n- or p-type respectively. As the charge carriers are
generated in pairs, the concentration n_i of electrons in the conduction band equals
the concentration p_i of holes in the valence band (n_i—intrinsic hole concentration
and p_i—intrinsic hole concentration) [26]. Typical semiconductors are group IV
elements and have 4 electrons in the valence shell. The energy gap (E_g) between
the conduction band and the valence band is known as the band gap and it has
no energy levels which are accessible for electrons to possess; see Figure 2.7 which
shows a layout of these bands. An external energy may excite an electron out of
the valence band across E_g into the conduction band. Such excitation creates an
electron-hole that carries on as a positively charged particle. Semiconductors have
energy gaps that lie roughly in the range 0.1 - 3 eV. The absorption of a photon
and excitation of electrons across the E_g occurs only if $E_\gamma \geqslant E_g$.

The p-type material has an excess of holes and the n-type has an excess of elec-
trons. Bringing these two material together in contact while keeping the two
grounded, you then get p-n junction solution. Applying a reverse bias across the
p-n junction will block electrical current flow. Under reverse bias conditions, the
voltage potential is connected negative to the p-type (acceptor atoms) material
and positive to the n-type (the donor atoms) material. This will increase the p-n
junction width due to a lack of electrons and holes and presents a high impedance
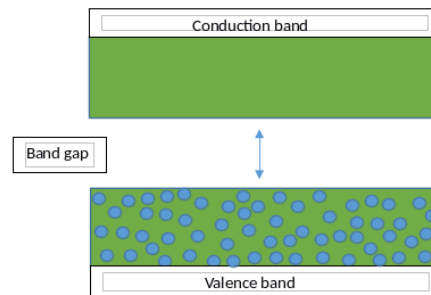
Figure 2.7 – Conduction band empty while Valence band is full with electrons.

path, almost an insulator. Holes in the p^+ region are attracted from the junction in the direction of the p contact, and electrons (e^-) in the n^- region are attracted from junction to the n contact, Figure 2.8 shows the formation of a depletion layer by charge diffusion, space charge density, electric field and built-in potential in a p-n junctions.
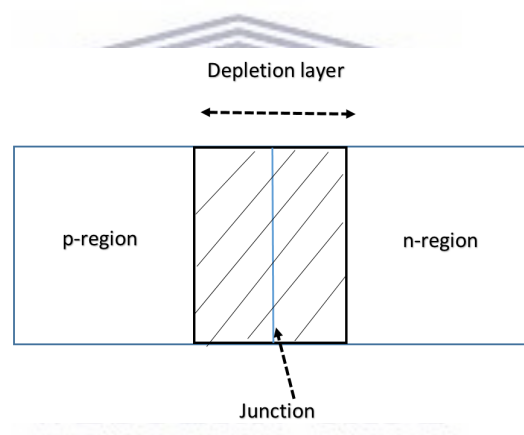
Figure 2.8 – Formation of depletion region in a semiconductor material.

The germanium material can be either p-type or n-type. These types all depend on the concentration of donor or acceptor atoms in the crystal. In order to connect the diode to an electrical circuit and amplify the signal output, contacts on the crystal are needed. The electrical contacts on the signal are thick, lithium contact, which is the $n+$ contact and $p+$ which is thin ion-implanted contact (Boron). The lithium contact is thick since it is diffused into the germanium. For n-type material, the thick lithium contact is placed on the inside surface while the thick ion implanted contact is placed on the outside surface; for the p-type the arrangement is reversed. For example, see Figure 2.9 and 2.10.

In an High-Purity Germanium (HPGe) detector, the p-type is placed as the cathode and n-type layer as the anode (p-i-n structure), the HPGe in between can be
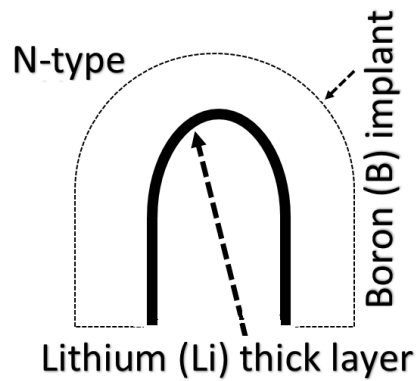
Figure 2.9 – Illustration of the HPGe N-type crystal.
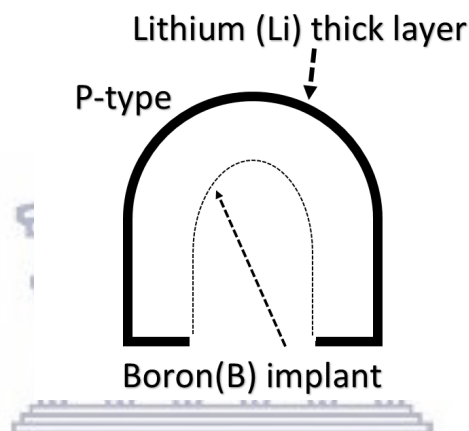
Figure 2.10 – Illustration of the HPGe P-type crystal.

effectively depleted of charge carriers (HPGe has an impurity concentration of 10^{10} atoms cm^{-3} instead of 10^{13} atoms cm^{-3}) [27]. The depletion can be obtained by applying a high voltage of up to 5 kV between the contacts, which are separated by a distance up to around 3 cm [28]. The narrow depletion layer at the junction of the germanium and the opposite contact impurity type gets expanded by a reverse-bias of high voltage application. When the voltage is increased, the depletion layer grows rapidly until it reaches the outer contact, causing the detector volume to be entirely depleted.

An operation voltage, V_0 is set at least in the 500 V range which is high enough in order to make sure a high charge mobility through the volume is maintained. For a depleted detection, the impurity ions can be seen as a fixed space charge distribution, ρ_s. Total electric field then results from the combined effects of the two, ρ_s and V_0. This electric field is weak on the side of the detector where two contributions have different signs and strong on the other [29]. In the coaxial

detection the field lines are concentrated in the inner contact due to the geometry. To concentrate this effect the type of the detector and polarity are chosen in such a way that the depletion starts from the outer contact. With a n-type crystal this can be obtained by putting the lithium-drifted contact on the inside and the ion-implanted contact on the outside. In use of the p-type detector, contacts are reversed. For the purpose of this work n-type HPGe detector was used. This type of detector is useful for many applications such as for studying high-energy γ rays. The HPGe n-type, co-axial detectors are at present the best γ-ray detectors in the energy range ~ 0.1 to ~ 10 MeV because of the high energy-resolution of the semiconductor Ge material, and the high full-energy efficiency of large detectors [30]. For typical nuclear structure experiments with high γ-ray multiplicities, such detectors are organized in large arrays.

Chapter 3

Theoretical background

3.1 Nuclear Decay

The internal conversion (IC) process competes with γ-decay emission. When a nucleus is excited from the ground state to an excited state, at some time later an excess energy will be released by some form of decay. Often, the nucleus will decay by γ-ray radiation. Nevertheless, in other cases, the virtual photon is released from the nucleus only to interact with one of the inner most orbital electrons and as a result, the virtual photon energy is transferred to the electron. Thus the nucleus is then said to have undergone IC. Figure 3.1 shows different ways in which the nucleus de-excites. The generic equation for internal conversion is $^{A}_{Z}X^* \rightarrow {}^{A}_{Z}X^{+1}$ + e$^-$, where $^{A}_{Z}X^{+1}$ is a ionized state and e$^-$ is one of the atomic electrons.

The Auger effect is a transition of an electron in an atom filling an inner shell vacancy causing the emission of another electron. When a core electron is removed from a core level (in other words electrons that are in the energy shells closer to the nucleus) of an atom, leaving a vacancy, an electron from a higher energy level may fall into the vacancy, resulting in the release of energy. Although sometimes this energy is released in the form of an emitted photon, the energy can also be used to remove an electron from the atom. This second electron ejected is known as an Auger electron [31], and this can consist of a number of vacancies in the atom orbits and thus emitted electrons.

For electron capture (EC) see Figure 3.2, nuclei having enough number of protons may pick up a free electron from one of the inner orbits which immediately couples with a proton in the nucleus to form a neutron and then emit a neutrino, conserving mass and energy. This process can lead to X-ray or Auger electrons emission. For

14

instance, in the process of IC and orbital EC, an electron leaves its atomic orbit and the vacancy is soon occupied. Here there are two processes competing; one is the emission of an X-ray which is due to the transition of an electron from an outer shell to the vacancy in a shell closer to the nucleus. The second one is that the energy difference between the orbits is not released as an X-ray instead the energy is used to knock out an electron from the orbit.
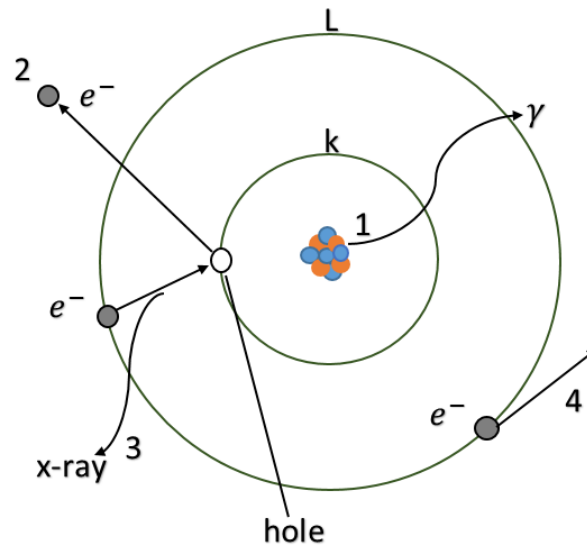
Figure 3.1 – A schematic of different ways to de-excite an atomic nucleus. The nucleus can be de-excited by γ-ray transition (labeled 1), but also by emitting a closely bound electron from the atom (labeled 2). Most of the time a K-electron is emitted, but an electron in the L-shell or higher shell can be also emitted. The electron hole that appears will soon be filled by another electron. This can result in the emission of X-ray photon (labeled 3), or the emission of an Auger electron (labeled 4).

The fundamental energy conservation relation governing the conversion electron energy is given by:

$$\mathrm{E}_e = \mathrm{E}_X - \mathrm{E}_B, \tag{3.1}$$

where E_e is the kinetic energy of the electron, E_X is the transition energy and E_B is the binding energy of the electron from the atom.

The competition of IC and γ-ray decay allows us to define the IC coefficient, α of a given γ ray as the ratio between the probability of the nuclear state decaying by IC (λ_e) or γ-ray emission (λ_γ) as follows:
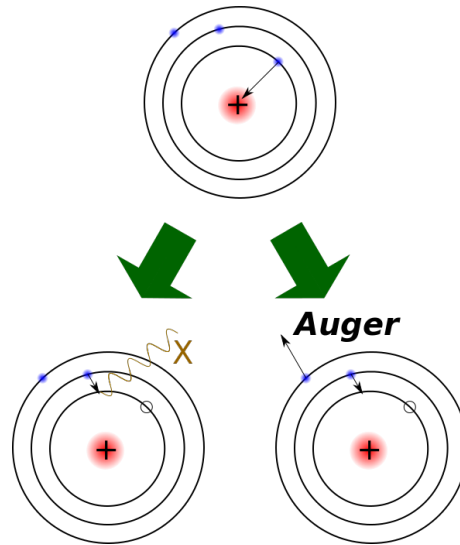
Figure 3.2 – Scheme of two types of electron capture. Top: The nucleus absorbs an electron. Lower left: An outer electron replaces the electron hole. An X-ray, equal in energy to the difference between the two electron shells, is emitted. Lower right: In the Auger effect, the energy released when the outer electron replaces the inner electron is transferred to an outer electron. The outer electron is ejected from the atom, leaving a positive ion [32].

$$\alpha = \frac{\lambda_e}{\lambda_\gamma} \tag{3.2}$$

IC electrons may be ejected from different atomic shells, giving rise to α_k, α_L, α_M, etc. Since the total probability of decay must equal the sum of the probability of decay via different path, using Equation 3.2 we can then define the total decay rate as follows:

$$\lambda_{tot} = \lambda_\gamma(1 + \alpha) \tag{3.3}$$

The coefficients can be calculated theoretically in electric and magnetic transitions using the equation below.

$$\alpha_i^L = Z^3 \Big(\frac{L}{L+1}\Big)\alpha_{fs}^4\Big(\frac{2m_e c^2}{E}\Big)^{L+5/2} \tag{3.4}$$

Here (i = K, L, M, N, ...), L is the multipole order, Z is the atomic number, m_e is the rest mass of the electron, E is the energy of the transition, and α_{fs} is the fine structure constant [33]. The above equation tells us that, the internal conversion coefficient increases with Z^3. This coefficient also increases for large multipoles, L.

However, there is another type of IC which is known as Bound Internal Conversion (BIC) which occurs between atomic states. In this process, a nucleus in an excited state will go through a transition to a lower-lying state with excitation of an electron to a formerly empty bound final state [34], when the binding energy of the converted electron is larger than the nuclear transition energy. BIC has recently been observed at GANIL in ^{125}Te [4].

3.2 NEET and NEEC

When an electron in the innermost shell is excited to an outermost shell, the electron can then de-excite in various ways. The electron can move from higher shell f to the lower shell i; this process will then emit a photon in the form of an X-ray. Alternatively, the transition energy can be transferred to one of the outer electrons; this will eject an Auger electron from the atomic shell. The third process, although its probability of happening is very small when compared to the first two, is called Nuclear Excitation by Electron Transition (NEET). The existence of NEET was first predicted by Masato Morita in the year 1973 [35]. In NEET, an electron from the upper level will flow into the vacancy. A virtual photon will be emitted which is then absorbed by the nucleus. This is possible only if the nuclear and atomic transitions have nearly the same multipolarity and matching energies.

A number of experiments have been performed looking for NEET in various isotopes. NEET has been successfully observed for the ^{197}Au [36], ^{189}Os [37] and ^{237}Np [38] isotopes. The most precise measurement in ^{197}Au was done by Kishimoto [36], who radiated a gold foil with monochromatic photons. In order for NEET to occur, the nuclear and electronic transition energy need to overlap. Moreover, Morita noted that NEET may be regarded as the inverse of Bound Internal Conversion (BIC) [35].

Probability of NEET: The probability of NEET taking place, P_{NEET}, is defined as the probability that the decay of the initial excited atomic state, i, will result in the excitation of and subsequent decay from the corresponding nuclear state. The expression for the probability of P_{NEET} is given by [39];

$$P_{NEET} = \left(1 + \frac{\Gamma_f}{\Gamma_i}\right) \frac{W^2}{\delta_{if}^2 + \frac{1}{4}(\Gamma_f + \Gamma_i)^2}, \tag{3.5}$$

where Γ_i and Γ_f are the initial and final atomic state widths, and W is the matrix element for the nuclear atomic coupling.

$$\delta_{if} = \Delta E_e - \Delta E_N, \tag{3.6}$$

with ΔE_e being the electron transition energy and ΔE_N being the nuclear transition energy.

P_{NEET} is very small when compared to P_{Auger} (the Auger electron emission probability) and P_{X-ray} (the X-ray emission probability). See for instance the list of theoretical and experimental probability calculations for these three different processes in Ref [40].

Nuclear Excitation by Electron Capture (NEEC) was proposed by V.I. Goldanskii et al. [41]. In the resonant process of NEEC, a free electron is captured by a bound atomic orbital state, as illustrated in Figure 3.3, with the binding energy plus the electron kinetic energy being equal to the energy of the first-excited nuclear state. In Figure 3.3 which shows the NEET and NEEC process the nucleus is initially in its ground state (G). For NEET the binding energy and for NEEC the free electron energy plus the binding energy is resonantly transferred to the nucleus and the nucleus becomes excited. NEEC is regarded as the inverse process of IC which results in an excited nuclear state that can decay either radioactively or by IC [42].

Despite the fact that there have been a vast number of theoretical studies performed on this subject, previous attempts to measure NEEC have been unsuccessful [16, 43]. A major challenge in the look for NPIs is the identification of a clear signature of the effect in an exceedingly disordered High Energy Density Plasmas (HEDPs) environment. Usually, the energy transfer on scales of keV is small and the signal of emitted radiation is weak compared to the background radiation in the HEDP.

3.3   Experiment design for NPIs

In this section, we discuss the design of an experiment that will allow accessing in electron mediated nuclear plasma interactions, the effect of NEEC or NEET.
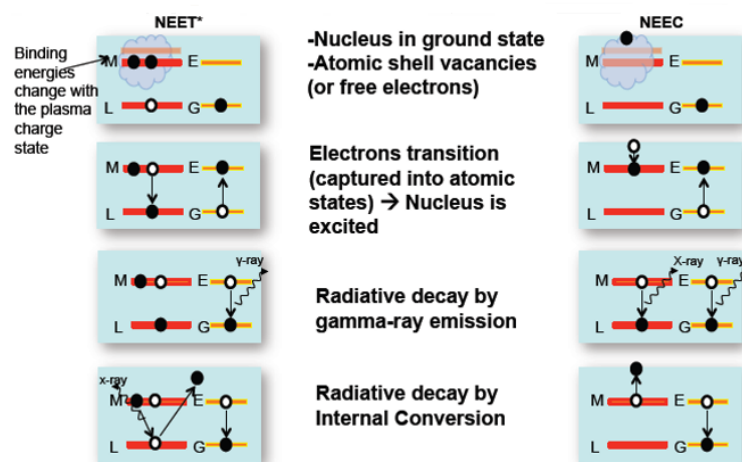
Figure 3.3 – Schematic of the NEET (left) and NEEC (right) processes. The red levels denote the atomic shells (L and M) and the yellow levels denote the nuclear excited and ground states (E and G). The top two boxes depict the excitation method while the bottom two show two different de-excitation schemes, drawings by A. L. Kritcher, LLNL [44].

The prepared target foils were irradiated using the 88-Inch Cyclotron accelerator facility of Lawrence Berkeley National Laboratory in Berkeley. Differential isomer population may be used to observe NPI effects in the HEDP plasma environment. The activation of ^{13}C occurring stable isotope with ^{197}Au heavy ion beam, results in the formation of unstable gold nuclei, ^{196}Au, ^{198}Au and etc. Reaction channels of ^{197}Au gold for the reaction of interest are given below:

^{13}C(^{197}Au, ^{198}Au*) reaction, the emission of γ rays comes from the composite nucleus by the unstable remaining residue nuclei, ^{198m}Au and the excited ^{198}Au nucleus. The unstable nucleus has a half-life of 2.3 days and undergoes decay by isomeric transition. It also has spin parity of 12^-. The excited residue nucleus, ^{198}Au has a half-life of 2.7 days and a spin parity of 2^-. The ^{13}C(^{197}Au, ^{196}Au*) reaction, resulting in an emission of two neutrons from the composite nucleus. The highly excited unstable nucleus, ^{198m}Au, has a half-life of 9.6 hours and a spin parity of 12^-. The excited residue ^{196}Au has a half-life of 6.2 days and a spin parity of 2^-. The resulting unstable gold isotopes may interact with the ^{209}Bi (bismuth) target (see the set-up of the targets in in Figure 3.5, 3.6 and 3.7). The ^{209}Bi isotope is one of the naturally occurring isotopes with high electron density number. In a highly electron-rich environment plasma, it is possible to resonantly excite a nucleus through energy with an electron [2]. Here ^{209}Bi foil target will act as an electron-rich environment plasma (see Figure 3.4) target which may allow for the interaction between the electrons and highly excited produced gold isotopes.

For the above reason, subsequently we expect that NEEC/NEET should occur in the created ordered plasma environment.

In the Close target shown in Figure 3.6, the beam should start off at about 14 % the speed of light and stops in about 40 microns of the target presented. This is the very roughly average time of < 1 ps. The lifetimes of the states in the quasi-continuum are on order of *femto* seconds. The beam stops before the nucleus has de-excited into the discrete states which tend to be close to *pico* seconds lifetimes, allowing time for highly-excited nuclei to interact with the ordered plasma. On the opposite side, the Far target is shown in Figure 3.7 the beam travels over a millimeter before encountering the ordered plasma. With 14 % the speed of light, this will then take about 24 ps, giving the nucleus more time to decay to the discrete states. There is a requirement that the energy of the electron, binding plus relative kinetic energy, should exactly match the energy of the nuclear transition. Hence in the discrete states, there is very little chance that there will be a state to excite to exactly as much as the electron energy.

The last target was the Blank target, which only consisted of the plasma-like environment. Here there was no thin target for reactions to take place. This target was a reference point of the other two targets used (Close and Far target). With the use of three targets, the Double Isomer-to-Ground State ratio (DIGS) will be investigated using section 3.4.
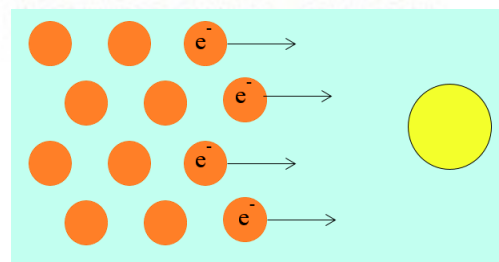
Figure 3.4 – For an accelerator beam, an ordinary target looks like an electron beam, an ordered plasma.
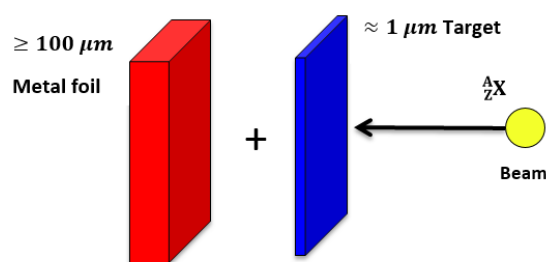
Figure 3.5 – Excited $^{A+1}_{Z}$X residuals made via binary transfer from thin target recoils into a thick metal foil which acts like a plasma target.
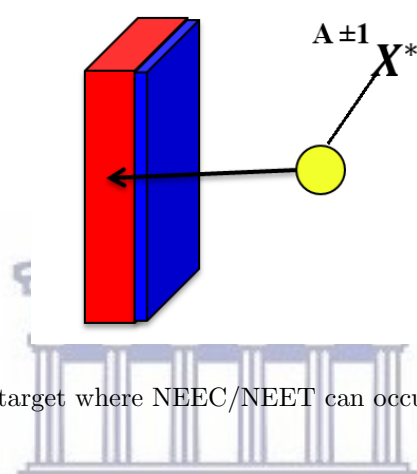
Figure 3.6 – Close target where NEEC/NEET can occur on quasi-continuum states.
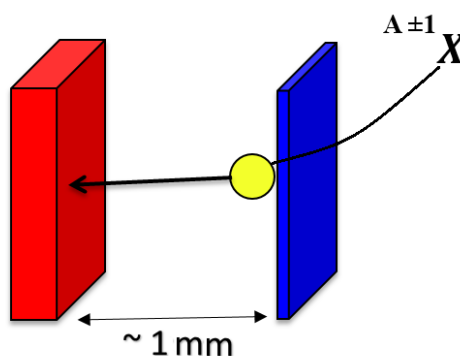
Figure 3.7 – Far target, the excited nuclei will decay to ground state or isomer, and NEEC/NEET will not occur in these states.

3.4 Change in Angular Momentum Distribution in Nuclear Plasmas

The distribution of highly excited states of emitted particles in a heavy ion collision can be represented by the following function [45, 46]:

$$\rho(J) \propto (2J+1)exp[-(J+\frac{1}{2})^2/2\sigma^2], \tag{3.7}$$

with $\rho(J)$ being the probability distribution of levels as a function of spin J, σ is a parameter which limits the population of high-spin levels and is in principle related to both the moment of inertia of the excited atom and its temperature [47]. The de-excitation from a specific spin level by a transition is assumed to populate residual spin levels with a probability dependent on the availability of the specific levels as illustrated by equation 3.7 (see Ref.[48]). The emitted particles in the reaction can be described by the following equation [49],

$$\sigma(J_c, E) = \pi\lambda^2 \sum_{S=|I-s|}^{I+s} \sum_{S=|J_c-s|}^{J_c+s} \frac{2J_c+1}{(2s+1)(2I+1)} T_l(E), \tag{3.8}$$

where $\sigma(J_c, E)$ is the cross section at spin J_c and energy E, λ is the de-Broglie wavelength of the incoming particle, s is the spin of the projectile, I is the spin of the target nucleus and $T_l(E)$ is the barrier transmission coefficient of a particle with orbital angular momentum l and energy E. A highly excited nucleus remains. These primary fragments are assumed to have an angular distribution function related to the nuclear level density [50],

$$N(J) = (2J+1)e^{-\frac{J(J+1)}{2B^2}}, \tag{3.9}$$

with the probability function often written as,

$$P(J) = P(0)(2J+1)e^{-\frac{J(J+1)}{2B^2}}. \tag{3.10}$$

where $P(0)$ is the density of levels with zero total angular momentum, B is approximately equal to the root mean square value of $(J+1/2)$ [48]. This functional form which was originally chosen from statistical considerations has, however, has also been predicted theoretically by J. R. Nix et al., [51] and by W. J. Sarantites et al., [52]. Excited nuclei in the continuum will decay through a γ-ray cascade with the assumption of dipole transition before it decays to the isomeric or ground state. Furthermore, parity must be preserved with cascade parity being assumed to be equal to a number that will always induce the same parity $(\Delta\pi)$ [47]. Each γ-ray decays to states given by the probability distribution equation 3.9, with the number of γ-rays in the cascade given by the following equation [51],

$$< N_\gamma > = (E_\gamma)^{\frac{1}{2}}/(l+1), \tag{3.11}$$

and here E_γ is the excitation energy of the nucleus. In this study lets assume the number of γ-rays emitted in the cascade to be equally three. This assumption is based on the model which was developed by J. R. Huizenga and R. Vandenbosch [47–53] although is found to range between 3 and 5 [48]. Following the γ-ray cascade and the consequent change in the angular momentum distribution given by $N(J)$, the nucleus will decay to the isomeric or ground state. Simulations predict that multiple NPIs will increase the angular momentum distribution see the article by D. L. Bleuel et al., [5]. The increase will affect the nucleus prior to the γ-ray cascade, impacting the end state of the nucleus. In conclusion, the isomer to ground state ratio will be perturbed, see Figure 3.8.
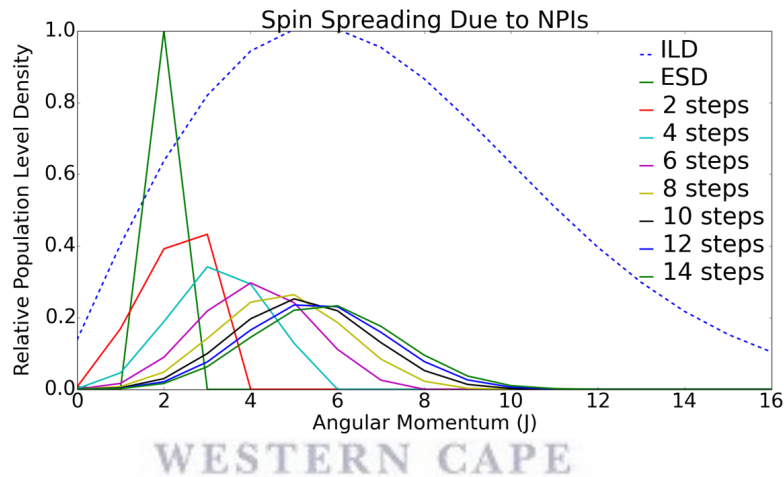
Figure 3.8 – This figure illustrates the distribution of total spin values of the compound nucleus due to NPIs. The blue dashed line represents the actual levels in the nucleus as a function of angular momentum, ILD stands for Intrinsic Level Density. The green spike represents a single initial excited state of $L = 2$, ESD stands for Entrance Sipn Distribution. The curve after that represents a model which randomly adds or subtracts angular momentum to that state proportional to the number of end states available. After two absorbed or emitted γ-rays, you would expect the red spin distribution. After four, the light blue, etc. The distribution quickly diffuses towards the natural spin distribution. Calculations by J. Escher, LLNL Nuclear Theory and Modeling Group [54].

3.5   Double Isomer-to-Ground State ratio

The interaction between highly-excited nuclear states and High Energy Density Plasma (HEDPs) environments such neutron and proton-rich astrophysical environment can profoundly effect nucleosynthesis (processes that are believed to have occurred immediately after the big bang). It is possible to excite a nucleus

through energy transfer from an electron i.e. in the process of NEEC and NEET discussed in section 3.2. The observation of a nuclear-plasma induced change in the isomer-to-ground state ratio would create the first observation of nuclear plasma interactions (NPIs) [55].

D. L. Bleuel et al. [5], proposed a new method to look for the effects of NEET and NEEC on highly-excited nuclei, which is the differential population of an isomeric state against the ground state of a de-excited nucleus. With the density of available nuclear states higher, the probability of a nucleus interacting with nearby electrons is thus greater, because of the high-level density and shorter lifetimes (larger widths) in the quasi-continuum, there is a much higher chance of there being some state or tail of a state that will match the electron energy. Our nuclei of interest will be produced by (n, γ) or (n, 2n) reactions with the help of a thin target. These reactions will initially populate states several MeV above and around the neutron separation energy (see Figure 3.9). The ratio of isomer to ground state decay will be measured in both cases. For instance, see the illustration of a plasma environment effect which is shown in Figure 3.9. This illustrates the creation of highly excited nuclei in the quasi-continuum, in an environment where there are free electrons (allowing for the potential of NPIs). In the quasi-continuum the level density is defined as the number of quantum levels per energy unit as a function of excitation energy [56].

In the quasi-continuum region level widths are small enough to allow NEEC and NEET processes to take place. With the new method, we expect NPIs effects, by inducing them on highly-excited, 1-5 MeV, nuclear states produced by the nuclear reaction prior to their decay by spontaneous γ-ray emission [5]. It is especially powerful while doing the measurement of this sort of ratios that the isomeric and ground state of the created isotope of interest goes on for a sufficiently long period of time (the samples must have high purity). It is necessary to limit the error sources (i.e. radiation and transportation times) which can contribute to the measurement results, in order obtain the accurate and reliable results.

Figure 3.9 shows the effect of NPIs in the quasi-continuum. The large density of nuclear states at the chosen range of MeV energies will increase the probability that energy from the atomic transition resonantly matches an available nuclear transition. The NPIs may change the angular momentum distribution [5], which then leads to a change in the subsequent isomer to ground state population. Finally, this will lead to a change in the isomer-to-ground state ratio when compared
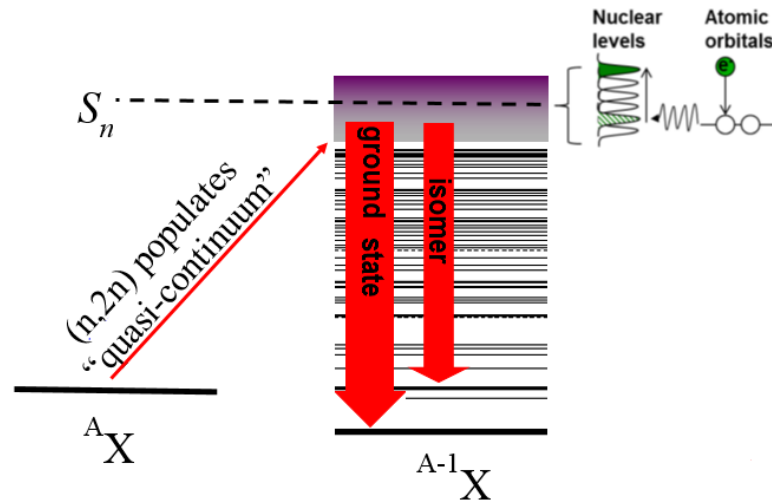
Figure 3.9 – Free electron is captured from the environment to the free atomic orbital, nucleus become even more excited possible modification in the high spins of the nuclei leading to a change in isomer to ground state ratio[5].

with the non-plasma environment. See also calculations for spin spreading due to NPIs by J. Escher in Figure 3.8 [54, 55].

To recognize the impact of NPIs to produce differential isomer population for reactions in versus out of a plasma environment, Equation 3.12 will be utilized [5],

$$R_{DIGS} = \frac{N_{iso}^{NPI} \big/ N_{ground}^{NPI}}{N_{iso} \big/ N_{ground}}, \tag{3.12}$$

where, N = number of states populated which is determined from its characteristic energy of γ-ray emissions measured in a high-purity germanium detector, NPI = Nuclear Plasma Interactions, and iso is short for isomer. The DIGS ratio compares isomer and ground state production in and out of plasma conditions, with the condition that $R_{DIGS} = 1$ implies that there are no plasma effects, but if $R_{DIGS} \neq 1$ then this may be a signature that there have been plasma effects.

Chapter 4

Experimental Setup

This chapter is organized as follows. In section 4.1 we review experimental details. In section 4.2 we give details about targets that were used during the experiment. In section 4.3 we discuss information regarding the 88-Inch Cyclotron and beam selection. Furthermore in section 4.4 we show graphical illustration during the time when the beam was on for all various targets used. In section 4.5 we discuss the counting process using HPGe detectors and chemical separation. We then close the chapter with section 4.6 where we discuss detection efficiency.

4.1 Experiment overview

The experiment was performed at the Lawrence Berkeley National Laboratory (LBNL), 88-Inch Cyclotron in Berkeley, CA, United State of America (USA). ^{197}Au beam was produced with 8.5 $\frac{MeV}{amu}$ beam energy. The ^{197}Au beam was used to radiate the thin $1\mu m$ thick ^{13}C foil target which was attached to an aluminum frame. For the Far target, three frames of aluminum were used with thickness of 2 mm each and the bismuth target used was 1 mm thick. From the set-up this gave a distance from the carbon foil to the bismuth foil backing to be 3 mm. For the Close target the set-up was similar except that they were two aluminum frame used. The Blank target were an aluminum frame with bismuth (same thickness as other targets) attached with epoxy. The ^{196}Au* and ^{198}Au* were studied using the ^{13}C $\left(^{197}\text{Au}, \ ^{196}\text{Au}^*\right)$ and ^{13}C $\left(^{197}\text{Au}, \ ^{198}\text{Au}^*\right)$ reactions.

26

4.2 Targets

In the experiment, three targets were used: Far target, Close target, and the Blank target. The Far target was constructed of a $2.3 \times 10^{-4} \frac{mg}{cm^2}$ ^{13}C foil attached to an aluminum frame of dimension $33.0 \times 33.0 \times 1.5$ mm. The aluminum frame had a centrical hole of radius 6.5 mm which the carbon foil completely covered, see Figure 4.1 and the sketch in Figure 4.2. The carbon foil was attached to the frame by floating the foil in a bath of deionized water and picking it up using the frame. This was done carefully to make sure no tearing of the carbon foil occurred. The Far target had an additional 1.5 mm thick aluminum frame with a hole with the same dimension as above as a spacer. The last frame was an aluminum frame which had a piece of bismuth (^{nat}Bi) 1.1 mm thick attached with epoxy.

Figure 4.1 – Far target(top) being removed after irradiation and blank target(below) before irradiation.
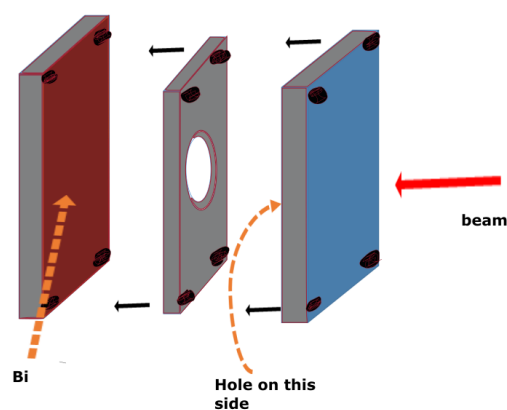
Figure 4.2 – Sketch of the Far targets, the is approximately 12.5 mm diameter.

For the Close targets foils of bismuth with mass 1.5 g and 1.7 g, ^{13}C was electro-plated to the surface of the bismuth forming a $2.4 \times 10^{-4} \frac{mg}{cm^2}$ thick layer, see the mounting in Figure 4.3, Figure 4.4, Figure 4.5 and the sketch in Figure 4.6.

In order to do this, a solution denoted by RF was made by combining 2.5 g resor-cinol, 3.6 g formaldehyde, and 88-liter acetic acid in 3.0 g dl (deciliter) of water. Then, 1.3 g ^{13}C powder was added to 8.0 g RF and sonicated to make a homoge-neous suspension. The suspension was allowed to gel at room temperature, then washed with acetone and allowed to air dry. Carbonization was then performed at 1050°C under a nitrogen atmosphere for 3 hour producing a monolithic carbon target. This carbon target was used to sputter-coat bismuth wafers in a Gatan precision etching and coating system (PECS). This instrument is equipped with a vibrating crystal microbalance to control and monitor deposition thickness. Bis-muth wafers were coated with the carbon target, these bismuth pieces were then attached to an aluminum frame using epoxy.

The Blank targets consisted of a spacer with no covering in the central hole and lastly an aluminum frame with the bismuth attached with the method previously described. The bismuth for the Blank targets were all of the same geometry with 1 mm thickness. In total two Far targets, two Close targets and two Blank targets were constructed. Each target was mounted on a copper plate, which was electri-cally isolated from the beam line and connected to a current integrator, measuring the total number of incident ^{197}Au particles.

The time profile of the beam was measured by the rate of fusion-evaporation neu-trons detected by a neutron monitor mounted outside the target and normalized using the total integrated current.
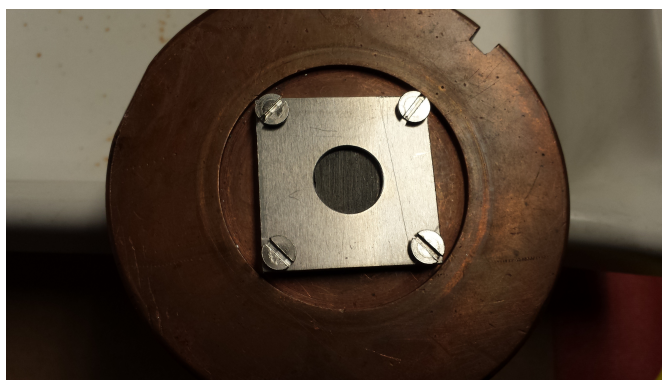
Figure 4.3 – Close target before irradiation mounted on a copper plate.
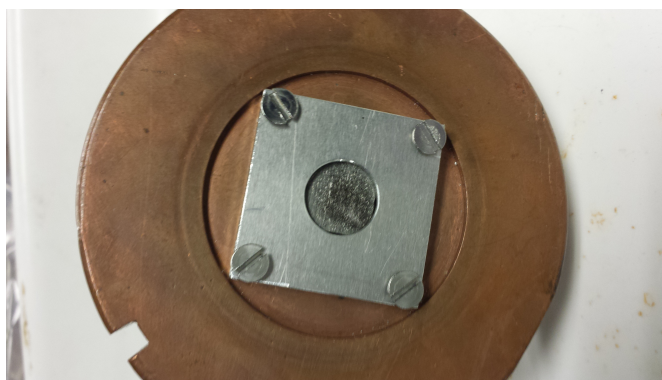
Figure 4.4 – Close after irradiation with Al plate.
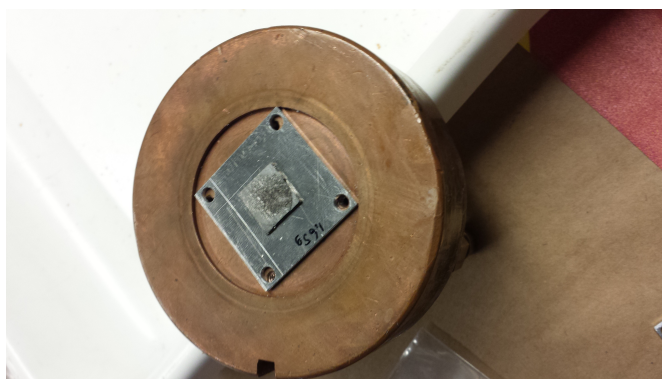
Figure 4.5 – Close with Al plate removed.
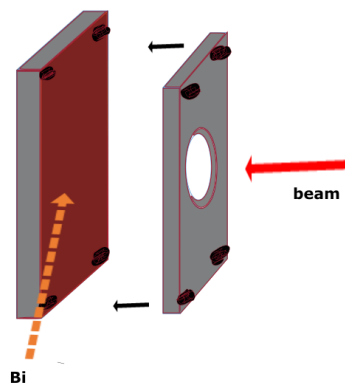
Figure 4.6 – For Close targets the above construction was used with the motivation because beam spot kept getting bigger (for example bigger than the hole in aluminum frame) hence aluminum frame was mounted in front of the Close target.

4.3   88-Inch Cyclotron and irradiation

The 88-Inch is a K = 40 sector focused cyclotron with both light and heavy-ion capabilities. Protons and other light ions are available at high intensities (10-20 $p\mu$A) up to maximum energies of 55 MeV (protons), 65 MeV (deuteron), 135 MeV (^{3}He) and 140 MeV (^{4}He) [57]. Major instrumentation at the 88-Inch Cyclotron include the Berkeley Gas-filled Separator (BGS), and the superconducting VENUS ion source, one of the most powerful Electron Cyclotron Resonance (ECR) ion sources in the world [58–60]. A layout of the ion sources at the 88-Inch Cyclotron accelerator facility is shown in Figure 4.7.
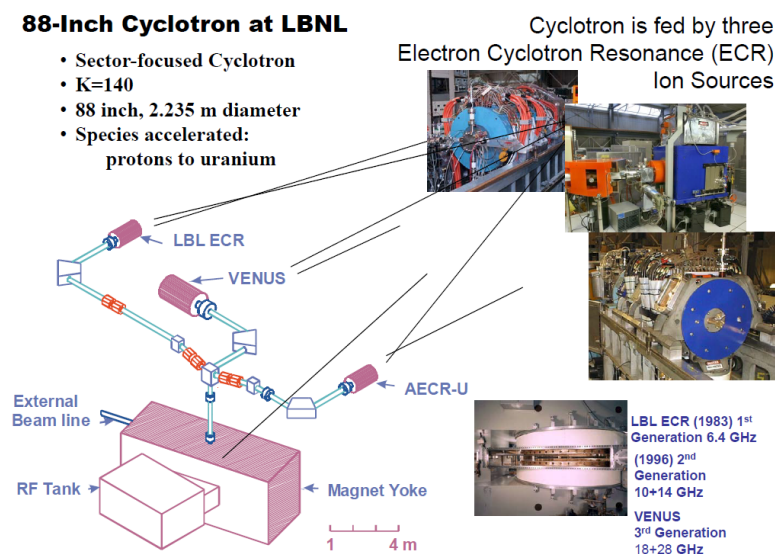
Figure 4.7 – Schematic layout of the ion sources of the 88-Inch Cyclotron accelerator facility [61].

A 8.5 $\frac{MeV}{amu}$ of ^{197}Au was provided by the cyclotron for four successive days. The current before the bending magnets was noted. Also the current hitting the target was acquired through a current integrator. Each target was in the beam for approximately 8 hours. They were then transported on a daily basis to the low background Nuclear Counting Facility (NCF) at Lawrence Livermore National Laboratory, Livermore, CA for chemical separation and counting.

4.4   Beam monitoring

In this section, we show the beam profile during the targets irradiation. First is the beam profile for the Far target followed by the Blank target beam profile and

lastly is a for the Close target.

Figures 4.8, 4.9 and 4.10 show the beam profile vs time, the beam profile was measured by the rate of fusion-evaporation detected in a neutron monitor mounted outside and normalized using the total integrated current. In Figure 4.8, which shows the Far target that was inside the chamber for ~ 385 minutes, it can be seen that the beam was relatively stable. Though in Figure 4.9 which shows Blank beam profile, irradiated for ~ 419 minutes the current was stable near 13 nA. Lastly, we have Figure 4.10 which shows Close beam profile and this target was inside the chamber for ~ 452 minutes. The beam here was not stable.
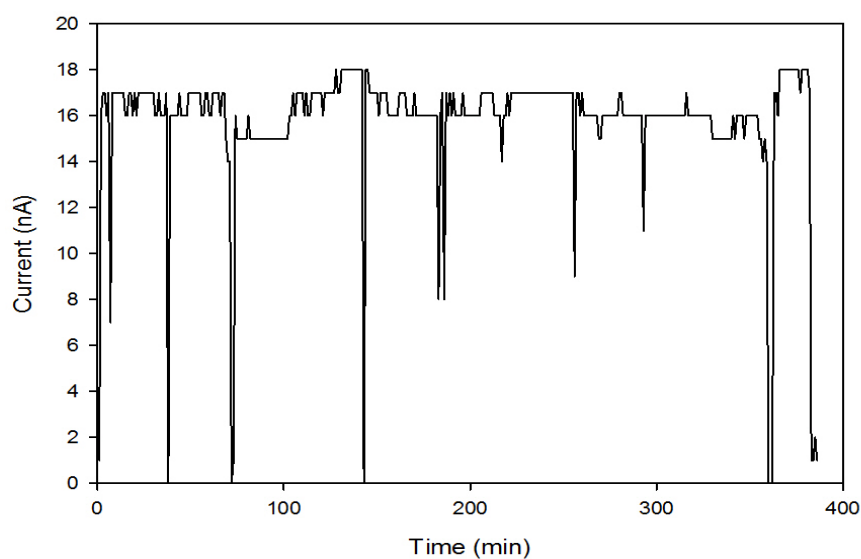
Figure 4.8 – Far target beam profile in a two dimensional plots with x-axis showing time (min) of irradiation and y-axis showing magnitude of the current in (nA).

4.5   Chemical Separation and Counting of Activated Samples

After irradiation at the 88-Inch cyclotron, the samples were transported to the low-background Nuclear Counting Facility (NCF) at the Lawrence Livermore National Laboratory (LLNL). The NCF is located one-and-half floors underground, with HPGe detectors surrounded in 10 cm of pre-WWII lead, minimizing contributions from environmental radiation. Each target was counted twice. The first count was
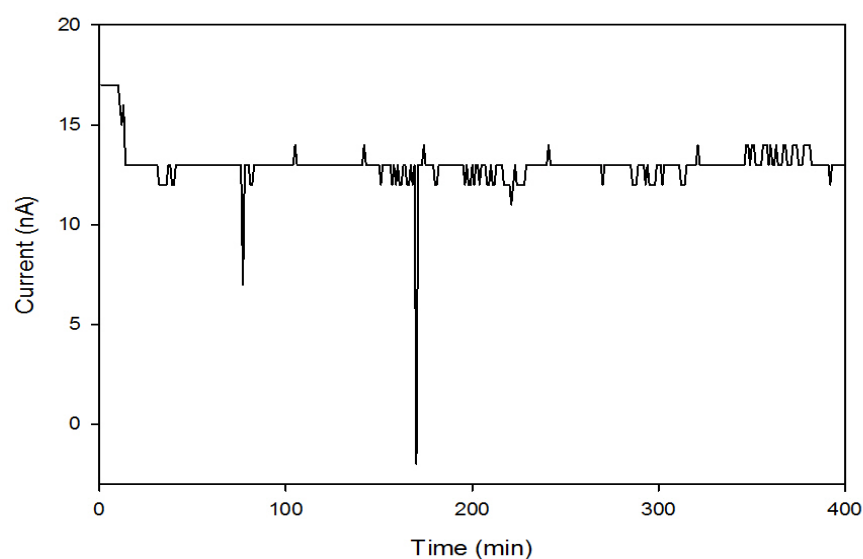
Figure 4.9 – Blank target beam profile in a two dimensional plots with x-axis showing time (min) of irradiation and y-axis showing magnitude of the current in (nA).
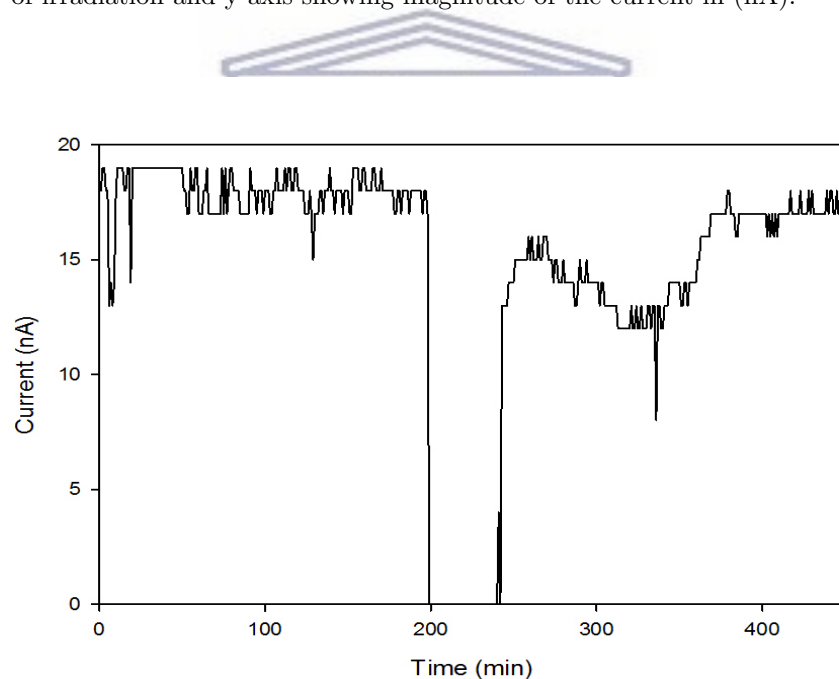
Figure 4.10 – Close target beam profile in a two dimensional plots with x-axis showing time (min) of irradiation and y-axis showing magnitude of the current in (nA).

before chemical separation of gold isotopes and the second count was after chemical separation of the gold isotopes. The GAMANAL software was used [62, 63] to interpret gamma spectra, perform background subtractions, and perform peak fits, correct for detector efficiency, sample geometry, dead time, coincidence loss, and self-shielding of γ-rays in the samples.

The detectors are regularly calibrated against National Institute of Standards and Technology (NIST) traceable multi-energy point sources and large area distributed sources. The gold was chemically separated because of big background contributions from fusion-evaporation residues. Each pair of carbon samples and bismuth samples were placed in a 40 mL centrifuge cone and dissolved with 2 mL 9M HCl 6 drops 8M nitric acid. The samples were placed in a hot-water bath under air streams and evaporated to dryness. Each sample was dissolved in 3 mL 6M HCl, and 2 mL of ethyl acetate was added. The mixture was agitated for 90 seconds on a Vortex mixer. The phases were allowed to settle, and the organic phase was transferred to a second 40 mL cone. Another 2 mL ethyl acetate was added to the aqueous phase, and the agitation was repeated. The resulting organic phase was combined with the previous 1mL 6M HCl was added to the organic phase and the mixture was agitated for 60 seconds after which the aqueous phase was discarded. The clean organic phase, containing the gold activity, was evaporated to dryness under an air stream, dissolved in 1M HCl, and quantitatively transferred to a Prindle counting vial in 10 mL of dilute HCl.

The chemical separation improved the signal-to-background ratio by a factor $\sim$ 100. The absolute efficiencies of separation, typically on the order of 90%, were determined individually for the foils by comparing the ^{196}Au activity measured before and after separation. Besides gold, isotopes of gallium, molybdenum, and antinomy could not be completely removed.

4.6   Detector efficiency

The GAMANAL program did not include detectors efficiency. To find these efficiency some calculation were performed using the γ-ray lines, 204 keV, 214 keV and 412 keV lines which are due to ^{198}Au and 148 keV, 188 keV, 285 keV, 316 keV, 333 keV, 356 keV and 426 keV which are due to ^{196}Au. Figure 4.1 below shows the out-put file of the far target counted for 480min from the GAMANAL program.

The information in Table 4.1 shows a typical GAMANAL output file for the Far target. These results are to be used to calculate detector efficiency. For example

Index	KEV	CALC. COUNTS	PROP. COUNTS	$\frac{PHOTONS}{MIN}$	$\frac{BKGNDCTS}{MIN}$	PCT ERROR	FWHM USED
1	55.850	802	906	9.473E+01	-	23.21	0.882
2	58.020	401	451	4.259E+01	-	42.16	-
3	59.564	1155	1297	1.146E+02	-	15.92	-
4	63.355	352	337	1.262E+01	0.3941	120.04	0.900
5	65.290	4722	4804	3.648E+02	-	4.15	0.801
6	67.043	9891	10037	7.268E+02	-	7.31	-
7	69.031	48419	48991	3.381E+03	-	2.08	-
8	70.952	81170	81903	5.423E+03	-	1.55	-
9	75.686	1982	2297	1.211E+02	0.3192	15.18	0.810
10	80.221	31755	31766	1.818E+03	-	2.98	0.969
11	82.675	9578	9549	5.323E+02	-	4.24	-
12	84.7206	387	384	1.104E+01	0.2457	56.28	-
13	87.206	132	134	3.570E+00	0.1383	202.49	0.661
14	90.004	1598	1582	8.174E+01	0.0577	7.27	0.905
15	92.693	789	896	1.863E+01	1.0006	40.06	1.017 -
16	97.337	2541	2549	1.268E+02	0.0554	4.58	0.815
17	100.141	298	292	1.470E+01	-	46.33	0.672
18	135.346	2000	2646	1.078E+02	-	10.79	0.827
19	140.506	18204	18195	9.111E+02	-	0.95	0.849
20	147.816	1627	1611	8.233E+01	-	6.80	0.833
21	158.400	3855	3838	2.008E+02	-	4.35	0.876
22	167.492	7236	7324	3.897E+02	-	2.35	0.867
23	180.704	3600	3975	2.110E+02	-	13.26	1.133
24	186.062	995	1008	4.059E+01	0.5939	14.49	0.938
25	188.197	1336	1351	7.667E+01	-	7.72	-
26	195.034	313	337	1.896E+01	-	28.44	0.899
27	197.357	995	1067	6.065E+01	-	9.71	-
28	204.099	1175	1219	7.050E+01	0.0508	10.69	0.880

Table 4.1 – GAMANAL out-put file for the Far target, counted for 480 min.

taking the average of calculated (CALC.) and prompt (PROP.) counts after dividing it by photons/min and the minutes of counts we get efficiency for the γ-ray line of interest i.e. if we take index 20 we have (1627+1611)/2 and divide it by 82, divide again by 480 you get 0.04. Thus, at 147 keV, the efficiency is approximately 4 %. This was performed for strong lines with low percentage (PCT) error and very low background subtraction (indicated by an -) from the output file.

To determine the efficiency uncertainty the error propagation method was applied. However, for some files the γ-ray line at 204 keV had a room background subtraction, for such files the efficiency were then obtained by the method of extrapolation. The efficiency of the germanium detectors is equal to the probability that the incoming photon gets absorbed in the charge depleted zone of the germanium crystal. Table 4.2 gives the results of the efficiency determination for the HPGe XP/3 model detector using the method described in section 4.6 of Chapter 4. Figure 4.11 shows the graphical illustration of the results in Table 4.2. Column 1 of the table below shows the energy of the γ rays in keV. The last two columns, illustrates the calculated efficiency of the HPGe XP/3 detector. This efficiency is actually the percentage of the γ rays which passed through the HPGe XP/3 model detector in the counting room after the activation of the samples.

keV	Average Counts	Photons/min	Eff. (10^{-2})	ΔEff. (10^{-4})
65	4763	365	2.72	6.50
67	9964	727	2.86	6.82
83	9564	532	3.74	8.94
148	1619	82	4.10	9.79
181	3788	211	3.74	8.93
193	1031	61	3.54	8.46
204	1197	71	3.45	8.77
214	2189	137	3.34	7.97
285	772	61	2.65	6.32
316	1123	97	2.40	5.74
333	1681	153	2.29	5.47
412	16309	1797	1.89	4.52
426	314	36	1.83	4.38
437	256	30	1.79	4.28

Table 4.2 – The relative detector efficiency for HPGe XP/3 model determined using the Far target with 480 min counting time.
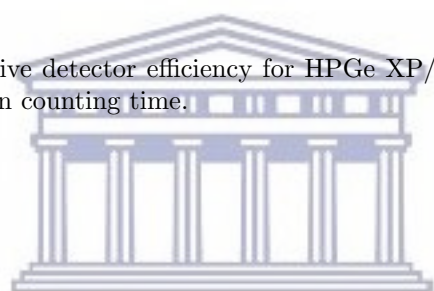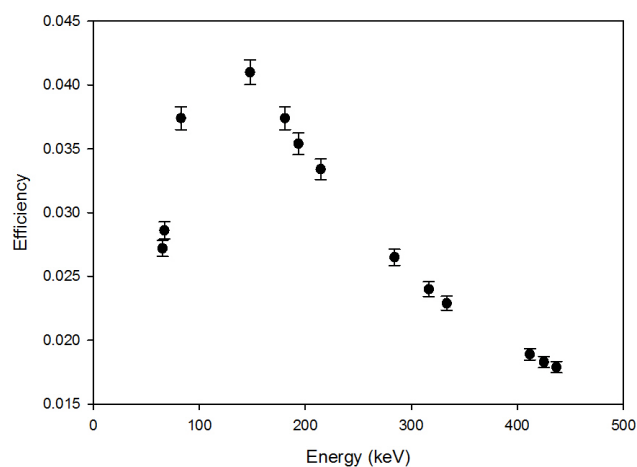
Figure 4.11 – The HPGe XP/3 detector efficiency curve produced from GAMANAL output and its error bars.

Chapter 5

Numerical analysis and Results

5.0.1 Calculation of DIGS

In this section, we discuss the way to calculate the Double Isomer-to-Ground state ratio (DIGS) with the acquired data for this project. The calculation of the DIGS was not straightforward. For example, some amounts of thallium and iridium were detected in the samples with approximately the same chemical separation efficiency as a gold isotope [64]. The ^{198}Tl decays by Electron Capture (EC) to ^{198}Hg comparative to the ^{198}Au. It produces the same γ-ray line but with the half-life of 5.3 hours. Moreover, the ^{198}Au ground state is also fed by the decay of its 2.3-day high-spin isomer at 812 keV. To get a correct number of counts of ^{198g}Au a disentanglement must be performed between growth and decay of the isomer and ground state in order to get pure ^{198g}Au number of counts. The analysis of interfering γ-rays and numerous decay chains were performed using linear algebra to decouple direct production of a daughter nucleus from in growth due to a parent nucleus. The decay equations that govern the experiment are given by the following set of equations;

$$\dot{N}_{iso} = -\lambda_{iso}N_{iso} + A.I(t) \tag{5.1}$$

$$\dot{N}_{ground} = -\lambda_{ground}N_{ground} + \lambda_{iso}N_{iso} + B.I(t) \tag{5.2}$$

$$\dot{N}_{iso} = -\lambda_{iso}N_{iso} \tag{5.3}$$

$$\dot{N}_{ground} = -\lambda_{ground}N_{ground} + \lambda_{iso}N_{iso} \tag{5.4}$$

36

with A and B being relative production parameters, these two parameters contain, σ the production cross-section and N_0 the number of target nuclei. λ is the decay constant, $I(t)$ is the beam current, N_{iso} is the number of isomeric state nuclei and N_{ground} represent the number of ground state nuclei. Full solutions to the above four equations can be found in Appendix A.

Isomeric decay schemes of ^{196}Au and ^{198}Au are shown in Figures 5.1 and 5.3, respectively, their level scheme following β-decay of the ground state in Figures 5.2 and 5.4, respectively. The decay scheme overview of the half-life times and the possible spin-parity. With the vertical distance representing changes in energy, the energy levels of the nuclei are represented by horizontal lines, these energies are measured in units of keV.
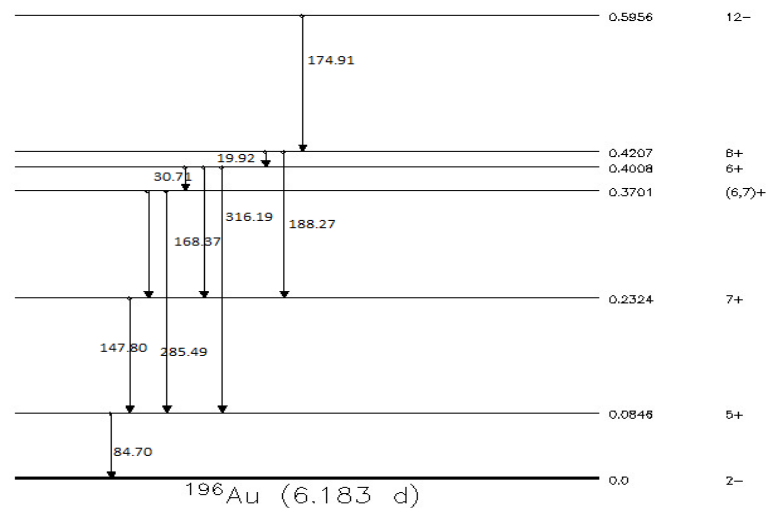
Figure 5.1 – ^{196}Au (12^-) isomer level scheme with half-life of 9.6 hours [65].
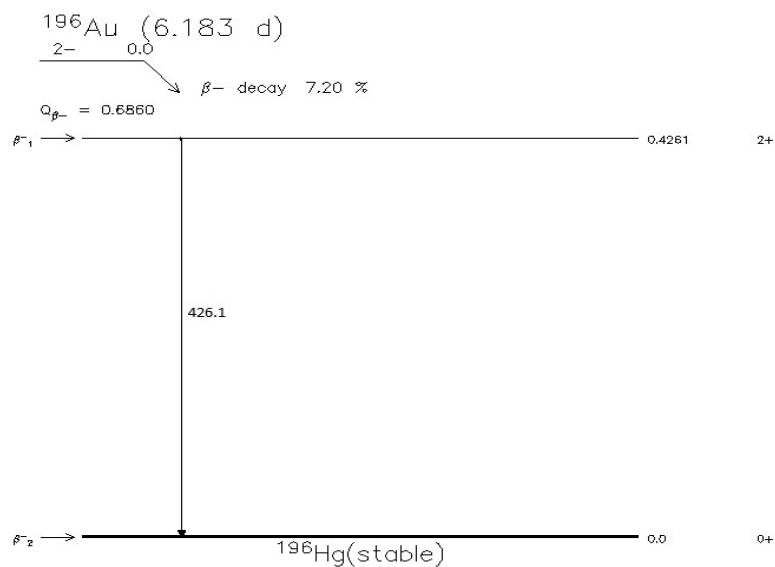
Figure 5.2 – ^{196}Au ground state level scheme following β- decay with half-life of 6.2 days [65].
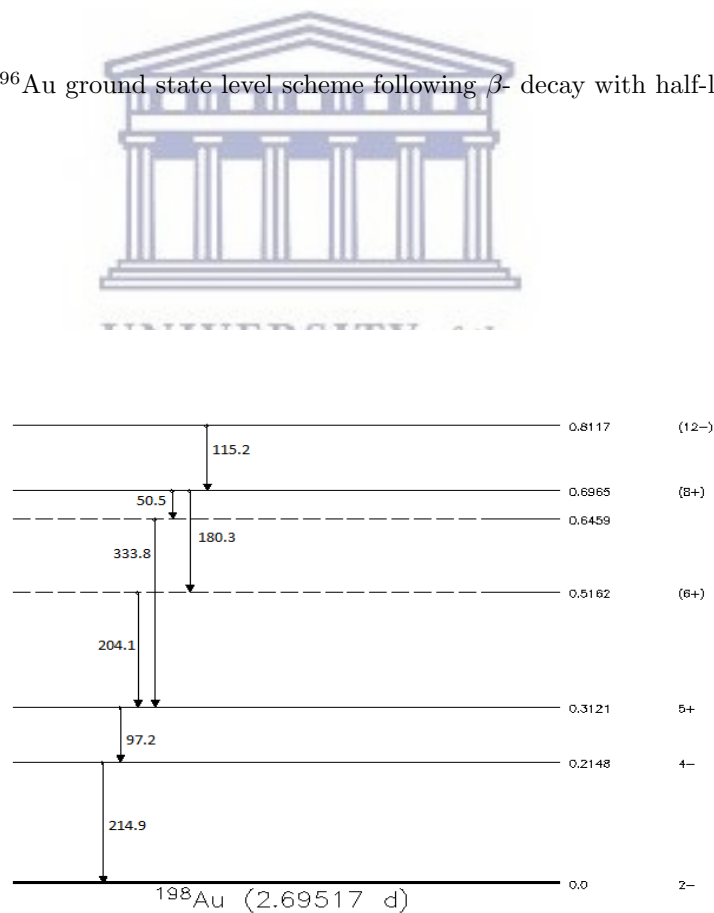
Figure 5.3 – ^{198}Au (12^-) isomer level scheme with half-life of 2.3 days [65].
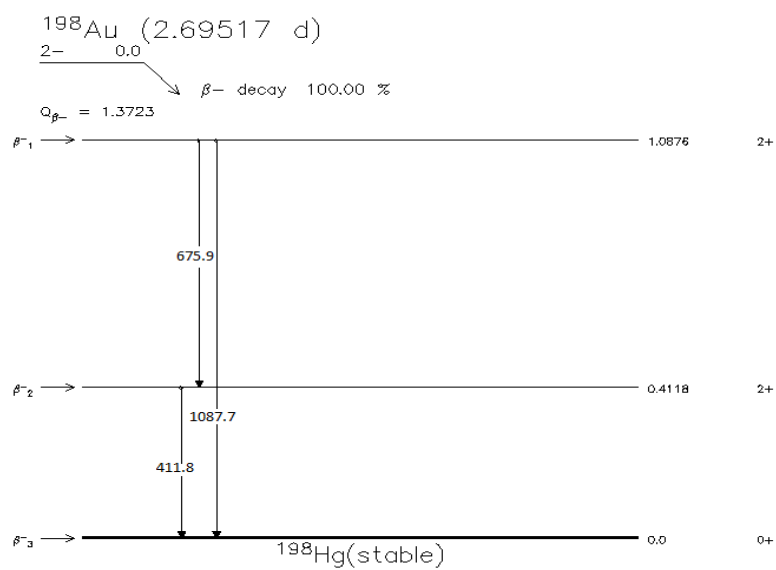
Figure 5.4 – ^{198}Au ground state level scheme following β-decay with half-life of 2.7 days [65].

Examples of Close and Far target γ-ray spectra for the ^{197}Au(^{13}C, ^{12}C) and ^{197}Au(^{13}C, ^{12}C2n) products with the different targets are shown in the following Figures 5.5, 5.6, 5.7 and 5.8 with some γ-ray peaks from the after-chemistry spectra which were used to calculate the Ground-to-Isomer state ratios. The far target spectra used can be found in Appendix B.
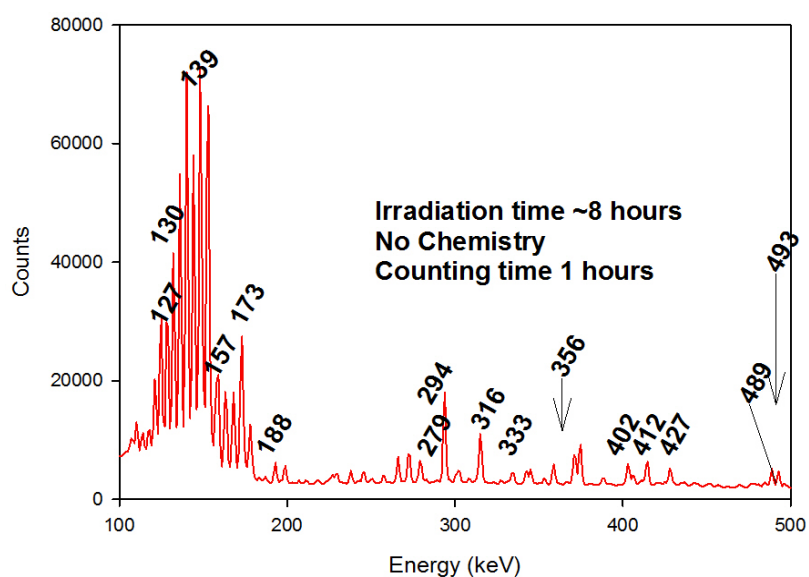
Figure 5.5 – Typical γ-ray spectra of the Close target before chemistry.
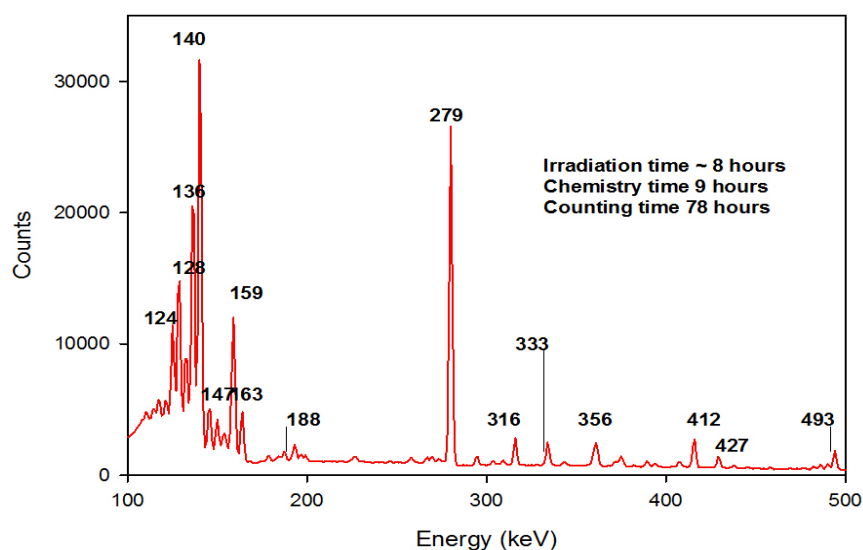
Figure 5.6 – Typical γ-ray spectra of the Close target after chemistry.
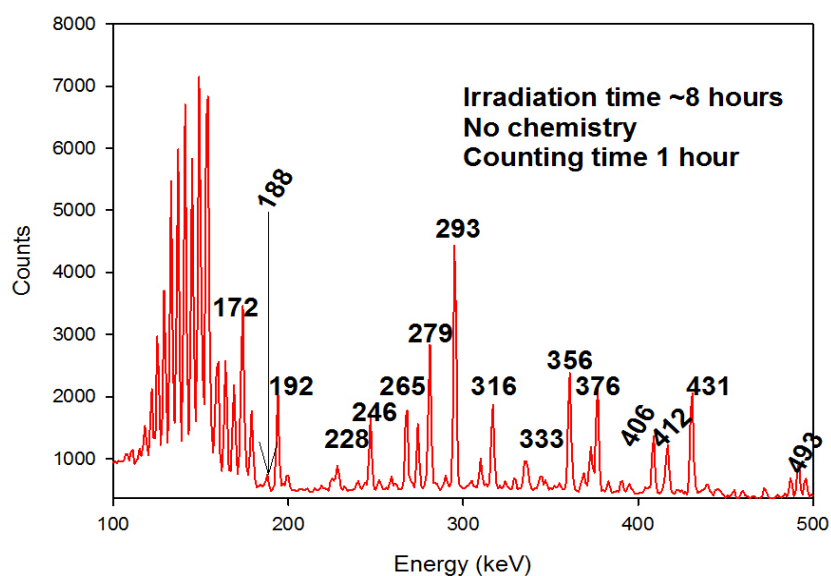
Figure 5.7 – Typical γ-ray spectra of the Far tagert before chemistry.
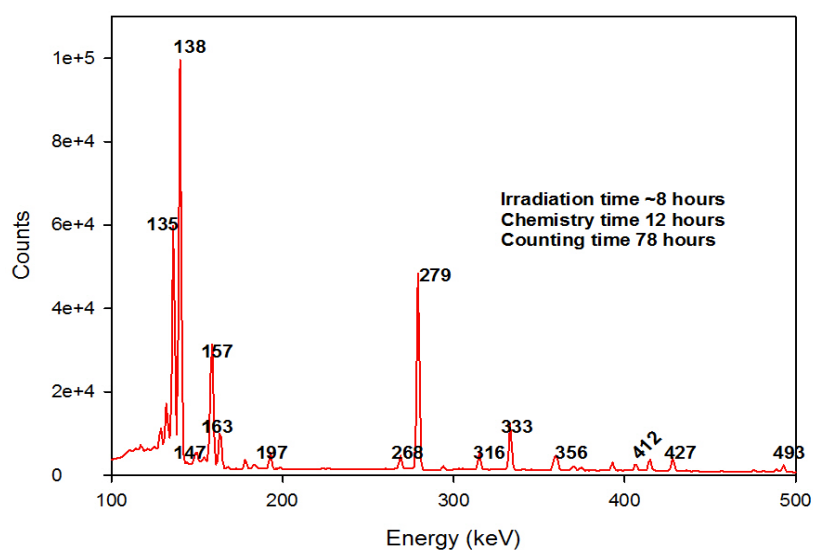
Figure 5.8 – Typical γ-ray spectra of the Far tagert after chemistry.

Figure 5.5 and 5.7 shows the Close and Far target spectra before chemical separation whereas Figure 5.6 and 5.8 shows spectra after chemical separation. It can be seen that after chemical separation peaks that due to contamination were removed, for example most indicated γ-ray lines are due to the de-excitation of ^{196}Au and ^{198}Au. The chemical separation goal was to ensure that the irradiated

samples were containing gold isotopes only. For more details on how chemical separation was done see section 4.5. Using data from the National Nuclear Data Center (NNDC) website and Table of Isotopes [65] the peaks originating from ^{196m}Au, ^{196g}Au, ^{198m}Au and ^{198g}Au could be identified.

5.0.2   Spectra Analysis

The RadWare package [66] is useful for the graphic display and for the analysis of one-dimension spectra i.e. peak area determination. The GF3 package is one of the RadWare software packages. This package was used successfully to measure photo-peak areas from the γ-ray spectra for this work. Two different methods were used to measure the areas, the first method calculates the γ-ray spectral peaks integrated counts by fitting data with Gaussian functions. Photo-peak backgrounds were approximated using photo-peak-width broadened linear step functions. This background is then subtracted by the program. The second method fits the photo-peak from the γ-ray spectra by the Gaussian function, here the background subtraction is done automatically by the program. The measured number of decays that occurred during counting were then corrected for efficiencies (see section 4.6 on to how efficiency for each γ-ray transition was calculated) of the detector and the intensities of the γ-ray transitions given in Table 5.1.

Both Figures 5.9 and 5.10 show the region where the strong peaks that are originating from the ^{196}Au and ^{198}Au isotopes are found. For more spectra on the blank target see section B.1 in Appendix B. Various criteria were used one after the other on the marked (red labeled) γ-ray lines. To search for impurities, all the marked γ-ray lines were investigated from the neighboring isotopes of ^{196}Au and ^{198}Au. The neighboring isotopes should not have similar γ-rays lines as the one marked if some dose. The half-life and intensities were carefully checked as to make sure the γ rays from the neighbors have no similar properties as the γ-rays in the ^{196}Au and ^{198}Au isotopes of interest. From these tests, very small amounts of Tl and Ir in their radiated samples were found. Moreover, the full-width-at-half-maximum height (FWHM) of a pulse height peak, which is used to measure the energy spread was also carefully checked when measuring peak areas of the marked γ-ray lines. The energy resolution of HPGe detectors is roughly 1.75 keV for γ-ray energies of 1.33 MeV. For any γ-ray line that gives an energy spread of greater than 1.75 keV we considered the possibility of the existence doublet containing photo peaks. For anything less than 1.75 keV we consider our detector resolution to be good, thus

we can measure the peak area and use it in the analysis. These checks also helped us to check for the overlaying of peaks during peak areas measurements.
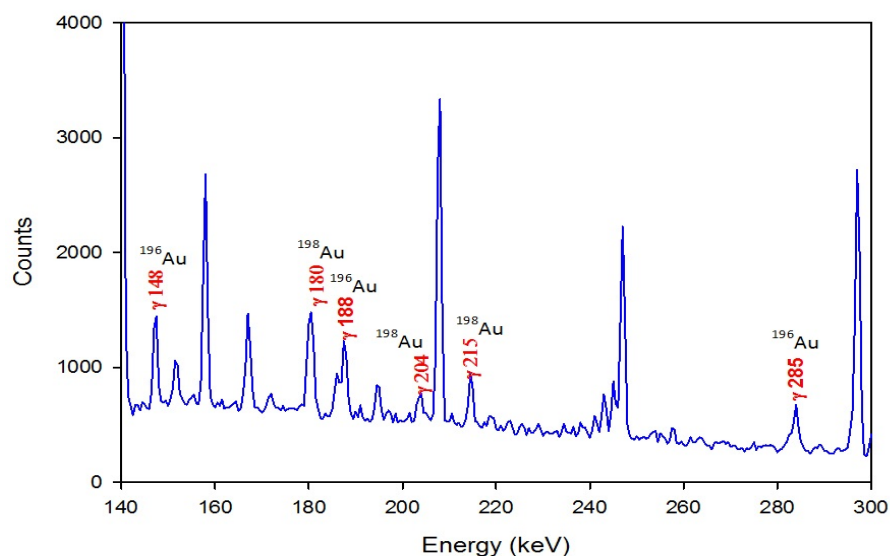
Figure 5.9 – Typical γ-ray spectra of the Close target after chemical separation zoomed in the region of isomeric decays for both ^{196}Au and ^{198}Au.
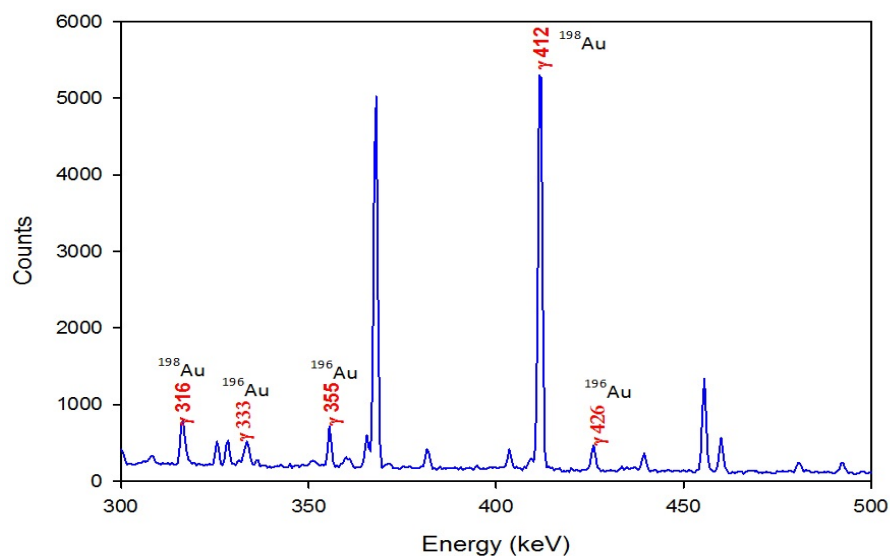
Figure 5.10 – Typical γ-ray spectra of the Close target after chemical separation zoomed in the region of the isomeric and ground state decays for both ^{196}Au and ^{198}Au.

Isotopes	Intensity(%)	Energy (keV)
^{196m}Au	43.5	147.81(2)
^{196m}Au	30.0(15)	188.27(3)
^{198m}Au	39(5)	204.10(6)
^{198m}Au	77.3	214.85(5)
^{196}Au	87	355.73(5)
^{198}Au	95.62	411.80(17)

Table 5.1 – Intensities and γ-ray lines for the ^{196}Au and ^{198}Au isotopes reported by NuDat Ref. [65].

The γ-ray energies and intensities used in this work were taken from NuDat [65], a resource available currently through the National Nuclear Data Centers (NNDC) online archives and these γ-ray energies and intensities are listed in Table 5.1. It provides an interface between web users and several NNDC nuclear structures and decay databases. NuDat can be used to search for ground and excited state level properties, γ ray information, and decay radiation information. In addition to the search capabilities, an interactive chart of nuclei is displayed [65].

In Table 5.2 and 5.3 (more data can be found in Appendix C) gives the measured peaks and errors of shown γ-ray energies in Table 5.1, respectively, which were used for DIGS calculations. As seen from the Tables 5.2 and 5.3 only few γ-ray lines peaks were measured in both the gold isotopes i.e. only the 147 keV and 188 keV which are from the isomer state and 355 keV from the ground state of ^{196}Au were measured and in the ^{198}Au only the 204 keV, 215 keV which are from the isomeric state and 412 keV from the ground state. To correct for efficiency and intensity the areas of the peaks measured in the GF3 program were divided by efficiency together with the intensity given for each γ-ray line. Changes in irradiation, transport or counting conditions of the samples can introduce errors in the correct number of counts that will be used in the analysis to compute production rates values. To figure out the uncertainties in the number of counts, the error obtained for each peak area θ was used to compute the lower and upper error bands i.e. θ-σ for lower error band and θ+σ for upper error band, σ is the peak area error. These qualities were combined according to the error propagation method when calculating the production rate values, with the estimate uncertainties from detection time detector ($\pm$ 86 seconds since the FORTRAN output rounding was to three decimal places) and for proton flux (0.5 nA was used).

Count.(h)	keV	Decays	Decays $_{lower}$	Decays $_{upper}$
12	147	192571	182135	203581
24	147	272167	259477	285446
36	147	314009	300072	328550
48	147	321991	307732	336856
60	147	328984	314097	344497
12	188	266211	237679	298824
24	188	379195	341605	421872
36	188	432063	390195	479485
48	188	459958	415750	509990
60	188	469793	424222	521386
12	355	253122	239267	268075
24	355	493263	473931	513676
36	355	713699	690305	738183
48	355	927350	900742	955038
60	355	1141350	1112057	1171703

Table 5.2 – ^{196m,196}Au decays for the blank target, first column shows the counting time by the detector for each gamma line in units of hours. The number of counts which were measured from the blank target used foils for the ^{196}Au isotopes were corrected for intensity and efficiency. The tables also show lower and upper error bands of the exactly measured decays. Decays for other different foils can be found in Appendix C.

In order to make sure that correct γ rays were used, the corrected number of counts were used. It can be seen from Tables 5.2 and 5.3 that the counts are increasing as the counting time in the detector increases. The result were then plotted against the time. Figure 5.11 shows the decay graph of the corrected counts from Table 5.3 for the 215 keV line.
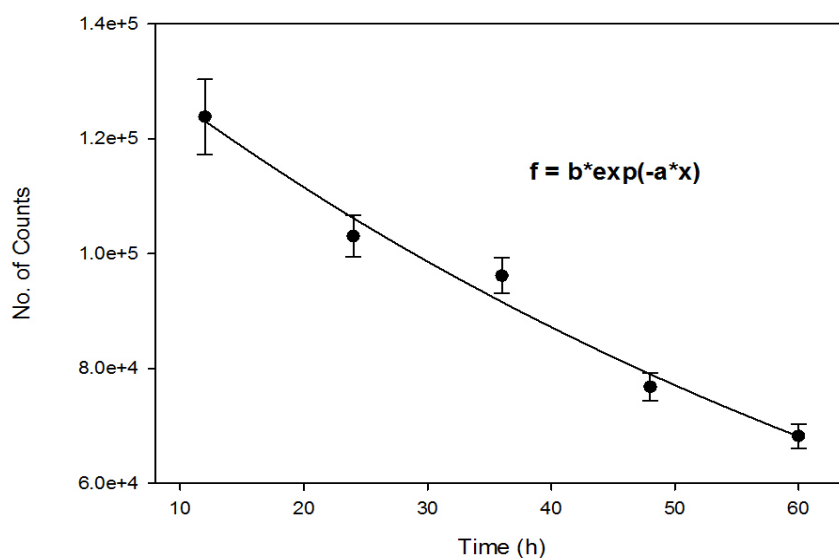
Figure 5.11 – ^{198}Au blank decay curve for γ line 215 keV.

Count.(h)	keV	Decays	Decays $_{lower}$	Decays $_{upper}$
12	204	127113	118183	136540
24	204	229971	216623	244059
36	204	329032	311908	347107
48	204	416706	396556	437975
60	204	486142	463535	510003
12	215	123826	117583	130376
24	215	226883	217190	237053
36	215	323037	310383	336313
48	215	399822	384850	415530
60	215	468045	451051	485874
12	412	1674687	1620166	1732288
24	412	2480410	2402293	2562862
36	412	3063216	2968367	3163330
48	412	3546154	3437526	3660811
60	412	3981218	3860250	4108899

Table 5.3 – ^{198m,198g}Au decays for the blank target, first column shows the counting time by the detector for each gamma line in units of hours. The number of counts which were measured from the blank target used foils for the ^{198}Au isotopes were corrected for intensity and efficiency. The tables also show lower and upper error bands of the exactly measured decays. Decays for other different foils can be found in Appendix C.

Theoretically the decay curve obeys the following equation,

$$f = b \exp(-\lambda x), \tag{5.5}$$

where b stands for the initial amount at time t and λ is the decay constant. Equation 5.5 was fitted using SigmaPlot [67] (a graphing and statistical analysis software package) together with the data in Table 5.2 and the value of b and λ was found to be 142766 ± 4797 counts and 0.0123 ± 0.0010 /h respectively. We can express the half-life, $t_{\frac{1}{2}}$, in terms of the decay constant as follows,

$$t_{\frac{1}{2}} = ln(2)/\lambda \tag{5.6}$$

Using the obtained value of a and plugging it into eq. 5.6 the half-life was found to be $t_{\frac{1}{2}} = 2.33 \pm 0.08$ days. The experimentally known value $t_{\frac{1}{2}}$ for the isomer state in ^{198}Au (12^-) is 2.27 ± 0.02 day [65]. It can be easily see that the calculated value is in agreement with the experimentally value, hence the values can be used in the analysis process. These decay curves were done for all other targets in order to verify photo-peak transition assignments.

To solve the Equations 5.1, 5.2, 5.3 and 5.4 the corrected number of counts for both ^{196}Au and ^{198}Au were labelled as D_{196m}, D_{196g}, D_{198m} and D_{198g} with m and g standing for isomer and ground state.

Using the data to produce some relative production rates of the isomer and the ground states. There are three different times of interest for this experiment. Let t_b be the time beam was shut off and t_c be the time when counting started and t_f be the final time when counting stops. For the experiment the well-known net rate of production-activated nuclei are given by the equations 5.1 and 5.2 from $t = 0$ to $t = t_b$ and Equation 5.3 with 5.4 from $t = t_b$ and $t = t_f$. These are coupled differential equations where N_{iso} decays into N_{ground}, thus $\lambda_{iso}N_{iso}$ is in equation 5.4; for $0 < t < t_b$ is the time of production.

This production is dependent on several factors but in the simplest case, the only factor that was non-constant was the beam current $I(t)$. Information regarding the beam current was acquired from the beam current reader from the control room. From this we now have $I(t)$ and what is unknown from the equations is A and B which are to be solved. To do this we need to calculate backwards in time from the end time t_f all the way to t_0.

The corrected number of decays D_{196m}, D_{196g}, D_{198m} and D_{198g} were measured from $t_c < t < t_f$. However the differential equations describe population. The first step of the solution to this problem is to calculate which population at $t = t_c$ would give the observed amount of decays during $t_c < t < t_f$. In order to perform the calculation the Runge Kutta 34 Method described in Appendix A was used; $f(t, y)$ will be the right hand side of equations 5.1, 5.2, 5.3 and 5.4, with the information from the control room our time step h for beam current was set to 1 minute.

5.1   Testing the code

To guarantee the nature of the created code, it is important to verify the correctness of the code. So to verify the software utilized, the code must be tried on theoretical predicted production rates keeping in mind the end goal to have full control over the inputs. This is the best way to be predict the consequence of the outputs and to see whether the functionality of the code give predictable outputs. To do this test, consider the accompanying simulation to test our code for this project. Suppose we were activating an X sample with the following reaction X (n,

γ) Y for a minimum time of $t_{irradiation}$ hours. Lets say after irradiation the sample is transported to the counting facility and we further assume this transportation takes $t_{transport}$ hours before it reaches the counting facility. Furthermore, assume the sample arrives at the counting facility and the counting is done with detector and a spectrum is accumulated for a counting time of some hours, long enough to get reasonable statistics for the counts in the photo-peaks. By measuring the counts in the peak of interest from the obtained spectrum i.e. γ-ray lines of the decay of some ^mY isomeric and ^gY ground state. Furthermore, suppose the relative intensities of the measured γ-ray lines are known and the absolute efficiency of the used detector is also known. Then the number of decayed nuclei can be expressed by the following formula:

$$D = \frac{C}{\epsilon \times I},\qquad(5.7)$$

where D is either for isomeric state or ground state, C is number of counts, ϵ is the γ-ray detection efficiency of the detector and I is short for intensity of the detected γ-ray. From the decay equations 5.8 and 5.9, N_0 can be calculated,

$$N_{iso} = AI(t) - \lambda_{iso}N_{iso}(t),\qquad(5.8)$$

$$N_{ground} = BI(t) - \lambda_{ground}N_{ground}(t) + \lambda_{iso}N_{iso}(t),\qquad(5.9)$$

where I (t) is the beam current recorded during irradiation time, $N_{iso,ground}$ are number of isomer and ground state nuclei at some time, t. The production rates A and B are given by the following relation:

$$A, B = N_0\Delta X\sigma\qquad(5.10)$$

where N_0 is the number of target nuclei after the radiation stopped at time $t = t_0$, ΔX is the thickness of the target and σ is the cross section of the reaction. Assume ΔX and σ are known, and the time intervals $[0, t_{irradiation}]$, $[t_{irradiation}, t_{transport}]$ and $[t_{transport}, t_{counting}]$ have been recorded. Then to solve for N_0 of the Y isotopes we need to solve the given decay equations 5.8 and 5.9 from $t_{counting}$ back to t_0. To test the MATLAB code in section D.1 of Appendix D if its working properly the two decay equations 5.8 and 5.9 were solved using Excel. The production rates

Testing parameters	
D_{iso}	1.000×10^5
D_{ground}	8.000×10^5
λ_{iso}	$7.702 \times 10^{-4}\ min^{-1}$
λ_{ground}	$9.623 \times 10^{-5}\ min^{-1}$
$t_{irradiation}$	$420\ min$
$t_{transport}$	$1500\ min$
$t_{counting}$	$3600\ min$

Table 5.4 – The Excel and MATLAB parameters that were assumed and used to test the code

were obtained by the Excel Solver (see Appendix E example of the spreadsheet used) program, these decay equations were rewritten in the following form:

$$N_{iso}(i+1) = N_{iso}(i)[\lambda_{iso}N_{iso}(i) + AI(t(i))]dt \tag{5.11}$$

$$N_{ground}(i+1) = [\lambda_{ground}N_{ground}(i) + \lambda_{iso}N_{iso}(i) + BI(t(i))]dt \tag{5.12}$$

for i = 1, 2, 3 etc. Table 5.4 shows the assumed values of decays of the Y isotopes, the irradiation, transport and detector counting times including the decay constants that were assigned for the some isomeric state and ground state. During irradiation time the beam current was assumed to be $\approx 17\ nA$. The ground state half-life was assumed to be 5 d and isomeric state to be 15 h. These values were used for both the MATLAB code testing and in Excel.

Figure 5.12 shows the graphical illustration of the isomer and ground state population after MATLAB and Excel output results by inputting the values in Table 5.4.

The solid and dotted black lines are the ground state population and the red solid and dotted lines are for the isomer population. Excel data points seem to lie below the MATLAB data points during the decay period after the stoppage of the irradiation of the sample. This difference is due to factors such as the numerical method used i.e. MATLAB function for the 4th Runge Kutta Method was used (see RK34 described well in Appendix A Section A.2). This method is more precise than the numerical way used in the Excel Solver. After using different cases in the decay lifetimes, both the shapes of MATLAB and Excel were behaving the same way as shown in Figure 5.12. The resulting production rates (A, B) of these cases are represented by Table 5.5.
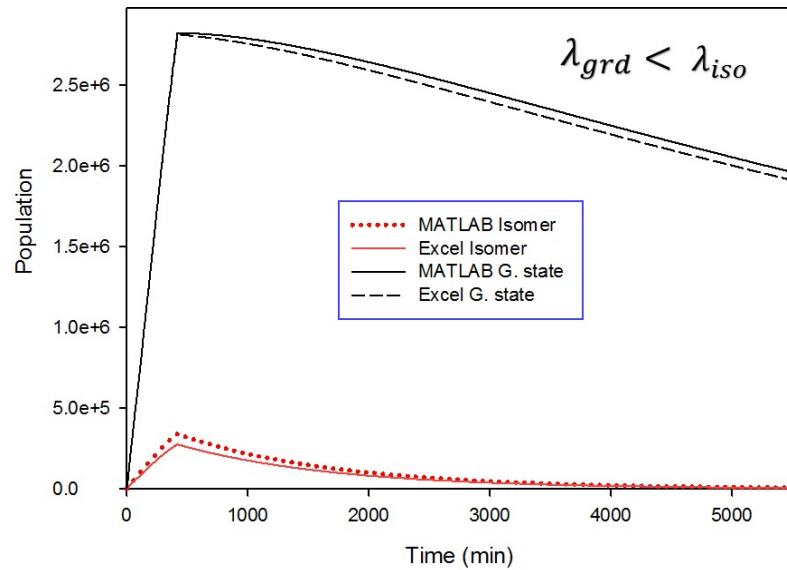
Figure 5.12 – Graphical results of the MATLAB and Excel Solver of the input parameters in Table 5.4 where D_{iso} and D_{ground} have halflife of 15 hours and 5 days respectively.

Production rates	MATLAB code	Excel Solver	Decay constant (min^{-1})
A_1	59.65	48.34	$\lambda_{ground} < \lambda_{iso}$
B_1	423.29	423.43	
A_2	48.38	46.79	$\lambda_{ground} > \lambda_{iso}$
B_2	372.88	305.87	
A_3	39.43	37.00	$\lambda_{ground} \simeq \lambda_{iso}$
B_3	285.70	270.38	

Table 5.5 – The production rate (dimensionless) values after three cases of changing the values of λ_{ground} together with λ_{iso}.

5.2 Algorithm to solve the decay equations

5.2.1 For $t_c < $ t $ < t_f$

Since nothing was feeding the isomer the population is easily translated into decays.

A developed MATLAB code in Appendix D was used, which iterates until the calculated decays matched the observed decays. The population of N_{ground} is not straight forward since N_{iso} is feeding it. It is then harder to relate the observed decays to a population. Because $N_{iso}(t_c)$ is determined, the number of decays that is due to the feeding effect can be obtained by solving equations 5.3 and 5.4 on the time interval $t_c < $ t $ < t_f$ with the initial conditions that $N_{iso}(t_c) = N^*_{iso}(t_c)$

(which is the previously computed) and $N_{iso}(0) = 0$. The decays that stem from the feeding effect is then given by $PartDecay = (N^*_{iso}(t_c) - N^*_{iso}(t_f)) - N^*_{ground}(t_f)$. Similarly the decays without feeding are given by the solution to equation 5.3 and 5.4 with the initial conditions that $N_{iso}(0) = 0$ and $N_{ground}(t_c)$ is some value. The decays from these sets of equation are $PureDecay = N'_{ground(}t_b) - N'_{ground}(t_f)$. The prime and the notation is to point out that they are the solution to the described equations and they are not the same. As before the initial values (in this case $N_{ground}(t_c)$) is iterated until it is correct and $D_{19X} = PartDecay + PureDecay$.

5.2.2   For $t_b <$ t $< t_c$

Using the calculated population at t_c, it is the easy to once again apply the Runge Kutta method and get the population at t_b through iteration (by iterating over values for $N(t_b)$ which result in the correct $N(t_c)$. Now the last step that remains is to compute value of the production rates A and B in equation 5.1 and 5.2.

5.2.3   For $0 <$ t $< t_b$

As before A and B were given through iteration. The population at t_b is known, the initial population is known (it is 0) and $I(t)$ is known. As previous steps, using equation 5.1 and 5.2, iteration (changing A and B) until this calculated population matches the previously computed population at t_b. When they match then A and B has been found hence the problem is solved entirely.

5.3   MATLAB results

The MATLAB code from Appendix D was used for calculating the A and B production rate, with given number of decays i.e. the corrected counts in Table 5.2, 5.3 and in Appendix C. Figure 5.13, 5.14 and 5.15 are example of how the population can vary over time when the current is not constant. The results seen are for ^{196}Au in the Blank, Close and Far targets (for ^{198}Au see section D.2 in Appendix D). All the counts used to produce these plots were counted over a maximum time of 48 hours using different detectors.
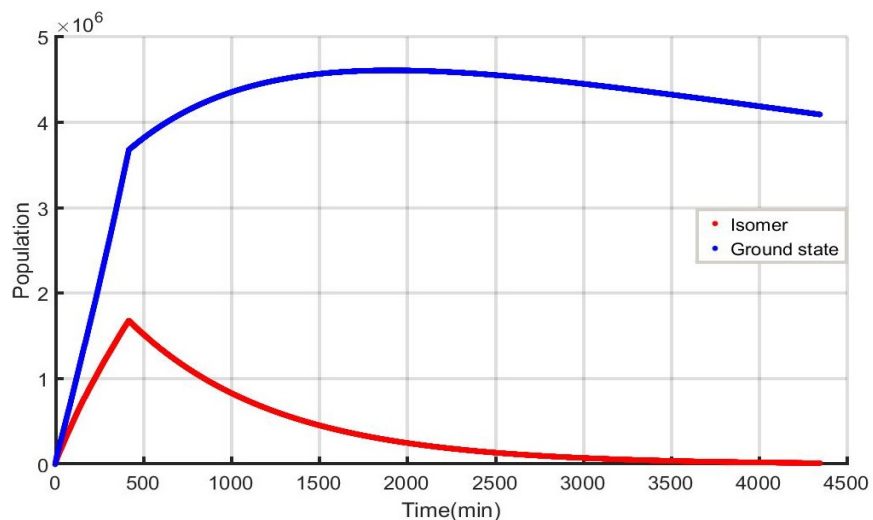
Figure 5.13 – Plot of population over time for ^{196}Au in the Blank target. The red line is the population of the isomer and the blue line is the population of the ground state.
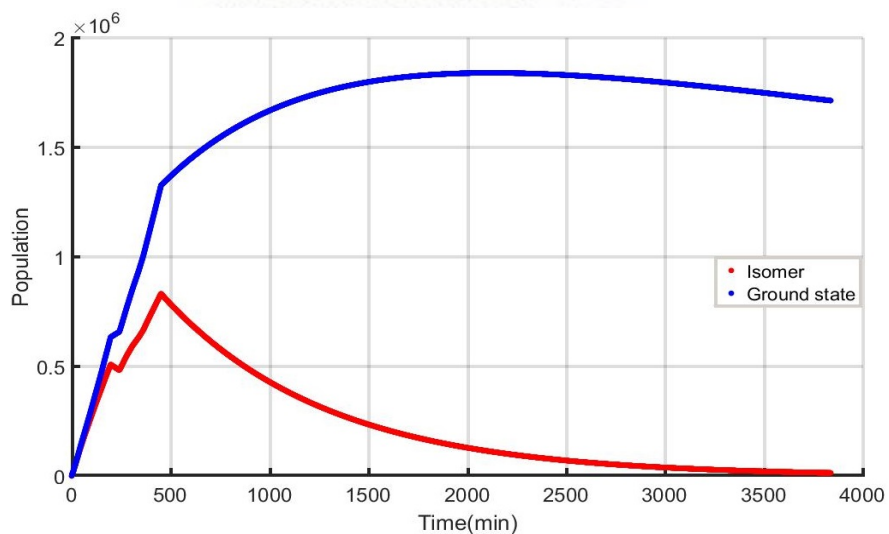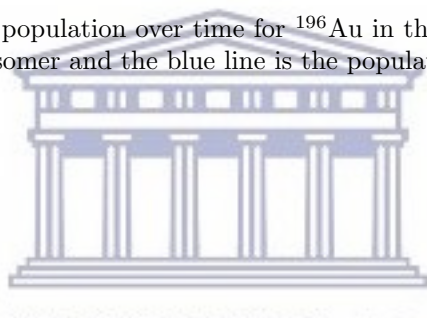
Figure 5.14 – Plot of population over time for ^{196}Au in the Close target. The red line is the population of the isomer and the blue line is the population of the ground state. The sudden change in population at 250 - 350 min is when the beam shut off.
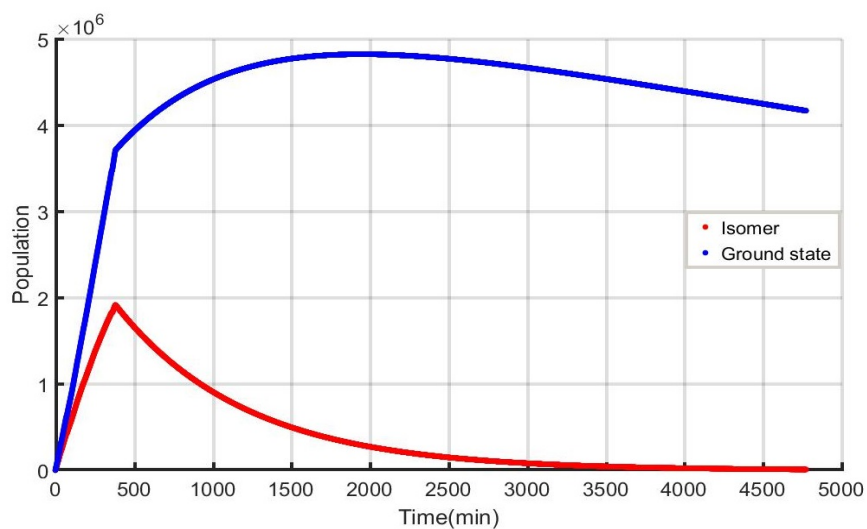
Figure 5.15 – Plot of population over time for ^{196}Au in the Far target. The red line is the population of the isomer and the blue line is the population of the ground state.

Chapter 6

Discussion and Conclusions

6.1 Discussion

6.1.1 Isomer and ground state production rates

Target	$\frac{E_\gamma^{isomer}(keV)}{E_\gamma^{ground}(keV)}$	A	B
Blank	148/356	$276.4^{+4.6}_{-5.5}$	$728.7^{+12.0}_{-14.7}$
Blank	188/356	$387.4^{+4.0}_{-2.5}$	$622.7^{+19.6}_{-21.7}$
Close	148/356	$78.2^{+3.0}_{-1.9}$	$238.3^{+29.4}_{-8.7}$
Close	188/356	$150.3^{+10.0}_{-6.5}$	$174.9^{+24.5}_{-5.4}$
Far	148/356	$25.5^{+2.5}_{-3.0}$	$680.6^{+13.2}_{-15.1}$
Far	188/356	$395.4^{+3.5}_{-6.4}$	$540.9^{+12.3}_{-24.0}$

Table 6.1 – ^{196}Au Isomer and ground state production rates (dimensionless).

Table 6.1 and 6.2 contains the production rates, A and B with the lower and upper error values. These production rates are the MATLAB derived values. The MATLAB results were used because the software could easily correct for the feeding of ground state population from the isomeric state. Included are the specific target foil that each of these individual values was extracted from and also the γ-ray lines that are due to isomeric and ground states. As seen from the R_{DIGS} plot in Figure 6.1, the value of A is much less than that of B for all the iterations. The value of A represents the isomer population and B that of

54

Target	$\frac{E_\gamma^{isomer}(keV)}{E_\gamma^{ground}(keV)}$	A	B
Blank	204/412	$217.0^{+1.9}_{-2.4}$	$2278.8^{+39.1}_{-47.8}$
Blank	215/412	$211.1^{+2.9}_{-3.6}$	$2281.6^{+38.5}_{-47.3}$
Close	204/412	$71.6^{+1.0}_{-1.5}$	$1113.8^{+11.8}_{-21.6}$
Close	215/412	$70.3^{+0.4}_{-1.4}$	$1114.1^{+11.8}_{-21.4}$
Far	204/412	$203.1^{+0.9}_{-1.3}$	$1687.2^{+20.8}_{-25.2}$
Far	215/412	$211.4^{+3.2}_{-3.3}$	$1682.9^{+19.4}_{-24.2}$

Table 6.2 – ^{198}Au Isomer and ground state production rates (dimensionless).

Target	R_{DIGS}	R_{DIGS_-}	R_{DIGS^+}
C/B	0.87	0.05	0.11
C/B	1.40	0.09	0.22
C/F	0.87	0.04	0.12
C/F	0.85	0.06	0.13
B/F	1.00	0.04	0.03
B/F	1.20	0.07	0.05

Table 6.3 – ^{196}Au Double-isomer to ground state ratios with its lower (R_{DIGS_-}) and upper (R_{DIGS_+}) error values for the three different targets.

Target	R_{DIGS}	R_{DIGS_-}	R_{DIGS^+}
C/B	0.68	0.03	0.02
C/B	0.68	0.03	0.02
C/F	0.53	0.02	0.01
C/F	2.00	0.10	0.10
B/F	0.79	0.02	0.02
B/F	1.40	0.05	0.04

Table 6.4 – ^{198}Au Double-isomer to ground state ratio with its lower (R_{DIGS_-}) and upper (R_{DIGS_+}) error values for the three different targets.

the ground state, see the MATLAB plots in Figure 5.13, 5.14 and 5.15 (also see section D.2 in Appendix D) the isomer population curve always lies below that of the ground state population curve. The difference indicates that the production of the isomer population is always less than that of the ground state population.

Table 6.3 and 6.4 contains the double isomer-to-ground state ratios (R_{DIGS}) for ^{196}Au and ^{198}Au isotopes, respectively. Included in them are the lower and upper error values. The obtained ^{196}Au and ^{198}Au isotope production rates values were used to compute the R_{DIGS} values. The R_{DIGS} values were carefully computed

with their lower and upper error values using the production rates of *Close* over *Blank* target foils, *Close* over *Far* target foils and last *Blank* over *Far* target foils. The chronological order used here to calculate the ratios is based on the theory of R_{DIGS}. A non-unitary value of the double isomer-to-ground state of *Close* over *Far* may indicate NPIs impact [5]. The last step in the chronological order is *Blank* divided by *Far* target foils. The reasons behind is that in the blank target the ^{197}Au beam was exposed to the ordered plasma environment (no thin carbon foil present). It is worth to see also section 5.1 for parameters which are contained in the production rates A and B. The other reason is that the γ-ray lines that are due to ^{196m,g}Au and ^{198m,g}Au were found in the data collected for this foil. This indicated a high number of nucleon-transfer reactions between ^{197}Au and ^{209}Bi. Most likely so high that (^{13}C, ^{12}C) and (^{13}C, ^{12}C2n) are small in comparison.
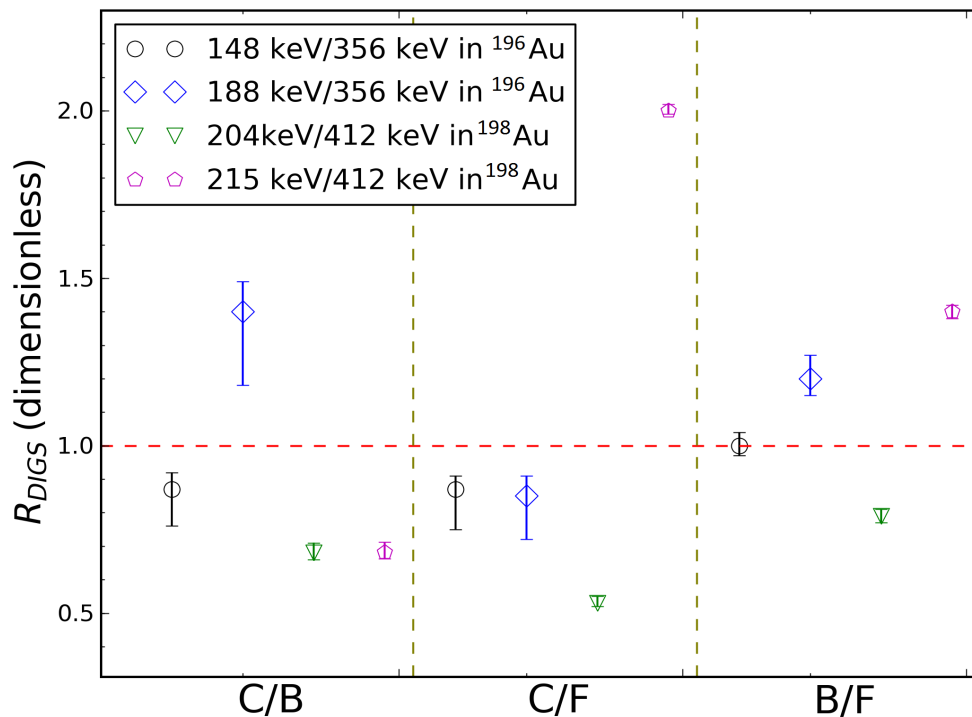
Figure 6.1 – Plot of the double isomer-to-ground state ratios (R_{DIGS}) for both the ^{196}Au and ^{198}Au isotopes for various targets. Along y-axis we have the R_{DIGS} values and along the x- axis we the regions of the different permutation of division of the targets. C is short for Close target, F is short for Far target and B is short for Blank target.

The tabulated R_{DIGS} values shown in Tables 6.3 and 6.4 were plotted on the same xy-plane see Figure 6.1. The experimental calculated R_{DIGS} values of ^{198}Au

isotope for the *Close* over *Far* and *Blank* over *Far* are quite off in range when compared with the R_{DIGS} values of ^{196}Au isotope except for one case in the region of C/B labeled on the x axis. The R_{DIGS} values for ^{196}Au are relatively closer to the standard unity value, which suggests that the nucleus of the produced isotope may not have been affected by the presented ordered plasma environment. A plausible explanation for the difference of the ^{198}Au isotope R_{DIGS} value, is that the ^{198}Au is fed by its high-spin isomeric state ($t_{\frac{1}{2}} = 2.3$ d and spin (12^-)) with a 812 keV γ-ray transition. This gives a clear signature that the data collected for the ^{198}Au should not be considered in our analysis, hence this gave a focus towards the collected data of the ^{196}Au isotope. Further, some small contribution from the ground state with half-life $t_{\frac{1}{2}} = 2.7$ d and spin (2^-) cannot be determined from the observation of the 412 keV γ line, because the energy of this line coincide with that of ^{198}Tl this is was discussed in the analysis section.

6.1.2   Determination of the Coulomb Excitation effects

However, to make sure that the result for the ^{196}Au isotope were suitable to use. Further investigation was done for possible effects that may have played a role during the reaction of the product with the electron plasma that was created using ^{209}Bi. Coulomb excitation effects were suspected to have possibly played some role. However, the feasibility of Coulomb excitation in a nuclear reaction is decided by the Coulomb barrier [68]. Coulomb barrier calculations were performed using the online calculator [69], for the three different projectiles (see Table 6.5) with the ^{209}Bi as a target. The first two projectiles were the ones produced after the two different reaction with the thin ^{13}C target (see experimental design in section 3.3) the isotopes produced were the ^{196}Au and ^{198}Au, respectively.

Moreover, the two produced isotopes were assumed to still have an energy of 1.2 or 1.4 GeV compared to the 1.7 GeV of ^{197}Au. This assumption is based on the effects that are described in chapter 2, which suggests different ways on how the beam loses energy when passing through a material. The last projectile was the ^{197}Au straight to the plasma environment (Blank target, no thin carbon target presented) with the energy of 1.7 GeV. The obtained Coulomb barrier (V_c) values obtained are listed in Table 6.5. It can be seen from the table that the average value of V_c is 670 MeV, with beam energies used, can see that the energy was always well above the Coulomb barrier. This indicates that there were more nuclear contributions or effects between the projectile and the target rather than

solely the electromagnetic interactions. Thus Coulomb excitation effects play such a minor role in the reactions and can be neglected.

Projectile	Target (ordered plasma)	V_c (MeV)
^{196}Au	^{209}Bi	670
^{197}Au	^{209}Bi	669
^{198}Au	^{209}Bi	669

Table 6.5 – The table represents the Coulomb barrier (V_c) for three reactions of the gold isotope as the projectile with the target plasma made of ^{209}Bi.

6.2 Conclusions

The essential aim of this thesis was to produce a code to disentangle isomer and ground state population, which will solve the sophisticated decay chains that were involved in the experiment. A MATLAB code has been created which solves the decay equation and gives out results of the production rates with the beam current not necessarily stable. The code likewise considers the feeding of the ground state from the isomeric state given by subtracting this contribution of isomeric states from the ground state number of decays. This is critical in light of the fact that the code provides the production rates output of the ground state population. The resultant production rates by the code were used to calculate the double-isomer-to-ground state ratios R_{DIGS}. The R_{DIGS} is introduced as a signature for detecting angular momentum distribution changes due to Nuclear Plasmas Interactions (NPIs) on highly excited states prior to gamma emission.

The R_{DIGS} were acquired for the two different gold isotopes ^{196}Au and ^{198}Au where for the ^{198}Au R_{DIGS} can be discarded due to the possible contaminants in the γ-ray spectrum as presented in the discussion section. The obtained ^{196}Au R_{DIGS} values deviate substantially from unity but there are large uncertainties due to the observation of a significant number of nucleon-transfer reactions on the bismuth target foil which appear to produce the isotopes of interest quite significantly. Moreover, due to the signal that was investigated which is expected to be very small to those produced in nucleon-transfer reactions on the bismuth, it prohibited an examination of the angular momentum distribution for the data obtained.

Further work that can be done in the future to improve the results of the R_{DIGS} such as to lower the beam energy below the Coulomb barrier of Bi. But lowering the energy will not produce a 12^- spin state [70]. Additionally, a heavier target

can be used but this is not practical because even for ^{238}U the Coulomb barrier is only 726 MeV which is below the beam energy. The method used here of R_{DIGS} is an intense technique for trying to figure out the NPIs effects on highly excited nuclei. In this regime, NPIs impacts are little to identify. Along these lines, further advanced experimental approaches treating the nuclear excitation mechanism in contact with ordered plasma environment presented needs to be developed. Strategies that would likewise permit little mistakes and have the capacity to disentangle angular momentum distribution effect impact because of NPIs.

UNIVERSITY *of the*
WESTERN CAPE

Appendix A

A.1

Analytical solutions to the decay and growth equations

The number of particles remaining at time t is governed by the following decay law equations for different conditions.

<u>Isomer</u>

$$\dot{N}_{iso} = -\lambda_{iso} N_{iso} \tag{A.1}$$

where λ_{iso} is the decay constant for the isomeric state, and this constant is $\propto t_{\frac{1}{2}}$ (half-life). This equation can be easily integrated to yield the following equation.

$$N_{iso}(t) = N_0 e^{-\lambda_{iso}t} \tag{A.2}$$

<u>Ground state</u>

$$\dot{N}_g = -\lambda_g N_g + \lambda_{iso} N_{iso} \tag{A.3}$$

rearranging the above equation as follows,

$$\dot{N}_g + \lambda_g N_g = \lambda_0 N_{iso} \tag{A.4}$$

multiplying by a integrating factor $e^{\lambda_g t}$, yield:

$$\dot{N}_g e^{\lambda_g t} + \lambda_g N_g e^{\lambda_g t} = \lambda_{iso} N_{iso} e^{-\lambda_{iso}t} e^{\lambda_g t} \tag{A.5}$$

noting the above that is a product rule, furthemore we use the separation of variables and integration which the gives the following results:

$$e^{-\lambda_g t}N_g(t) - N_g^0 = \frac{\lambda_{iso}}{\lambda_g - \lambda_{iso}}N_{iso}[e^{(\lambda_{iso}-\lambda_g)t} - 1] \qquad (A.6)$$

where N_g^0 is the ground state initial amount multiplying both sides by $e^{-\lambda_g t}$,

$$N_g(t) = N_g^0 e^{-\lambda_g t} + \frac{\lambda_{iso}}{\lambda_g - \lambda_{iso}}N_{iso}[e^{-\lambda_{iso}t} - e^{-\lambda_g t}] \qquad (A.7)$$

Assuming the half-life of the isomeric state is less that the half life of the ground state, the overall result is that the number of nuclei of the isotope will decrease exponentially according to its own half life. The following two equations cannot be solve analytical.

$$\dot{N}_{iso} = -\lambda_{iso}N_{iso} + A.I(t) \qquad (A.8)$$

$$\dot{N}_{ground} = -\lambda_{ground}N_{ground} + \lambda_{iso}N_{iso} + B.I(t) \qquad (A.9)$$

where A and B are production rates containing the number of target nuclei after irradiation time, the thickness of the target and cross-section of the reaction, I(t) is the proton flux. For the above two equations, if $I(t)$ is constant the two can be solved in a similar way as the first two equations [71]. Otherwise, if $I(t)$ keeps changing then a numerical approach is the best tool to use, an example can be seen from figure 13, 14 and 15 which shows $I(t)$ vs t. It can be easily spotted that $I(t)$ is not a simple function as the beam current is fluctuating, hence a numerical approach is needed to be used.

A.2

Numerical solutions to the decay and growth equations

The 4th order Runge Kutta (RK34) numerical method is suitable to solve the above 4 decay and growth equations.

Runge Kutta In general, consider the following equation where the right-hand side is a function of time and the left-hand side is another function that depends on time.

$$\frac{dy}{dt} = f(t, y), y(t_0) = y_0 \tag{A.10}$$

Here the task is to solve the above differential equation, that is; given the function $f(t, y)$ find the function y(t) such that it passes through the point (t_0, y_0), whose derivative is the given function. The RK34 formulation is as follows [72];

$$y_{rk1} = f(t_n, y_n) \tag{A.11}$$

$$y_{rk2} = f(t_n + \frac{h}{2}, y_n + \frac{h}{2_{rk1}}) \tag{A.12}$$

$$y_{rk3} = f(t_n + \frac{h}{2}, y_n + \frac{h}{2_{rk2}}) \tag{A.13}$$

$$z_{rk3} = f(t_n + h, y_n - hy_{rk1} + 2hy_{rk2}) \tag{A.14}$$

$$y_{rk4} = f(t_n + h, y_n - h_{rk3}) \tag{A.15}$$

$$y_{n+1} = y_n + \frac{y_{rk1} + 2y_{rk2} + 2y_{rk3} + y_{rk4}}{6} \tag{A.16}$$
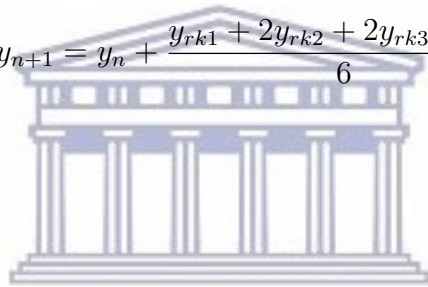
Appendix B

B.1

Blank and Far spectra
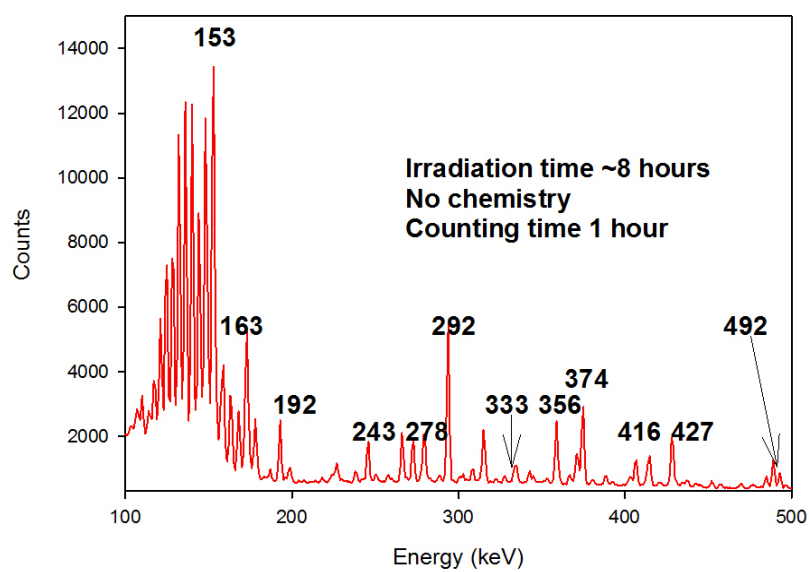
Figure B.1 – Typical γ-ray spectrum of the Blank target before chemistry.
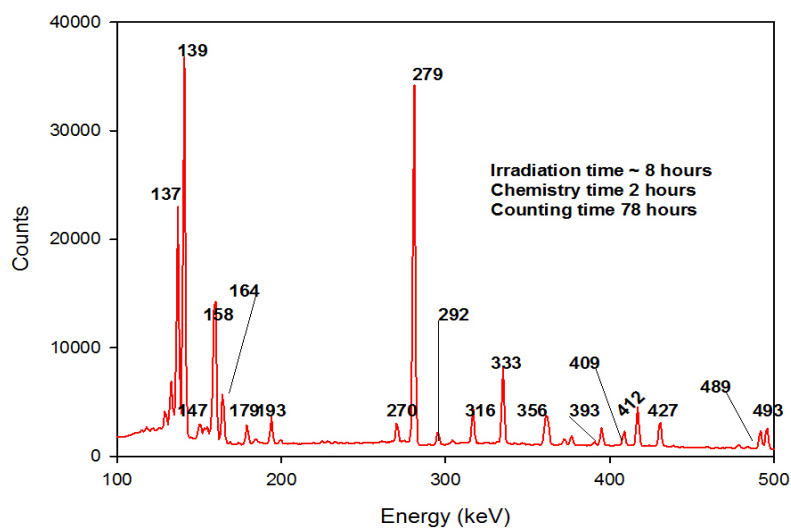
Figure B.2 – Typical γ-ray spectrum of the Blank target after chemistry.
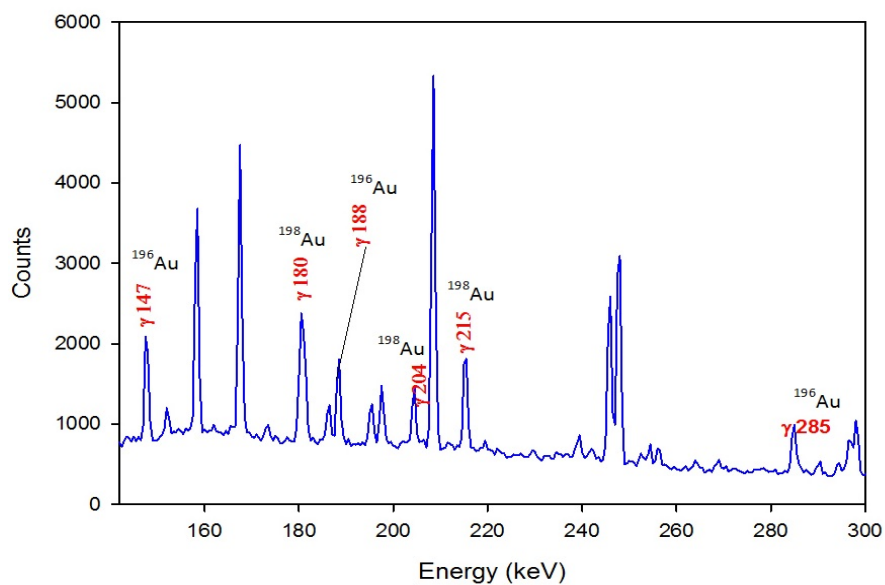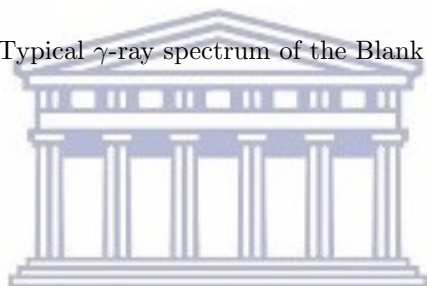
Figure B.3 – Typical γ-ray spectrum of the Blank target after chemical separation zoomed in the region of isomeric decays for both ^{196}Au and ^{198}Au.
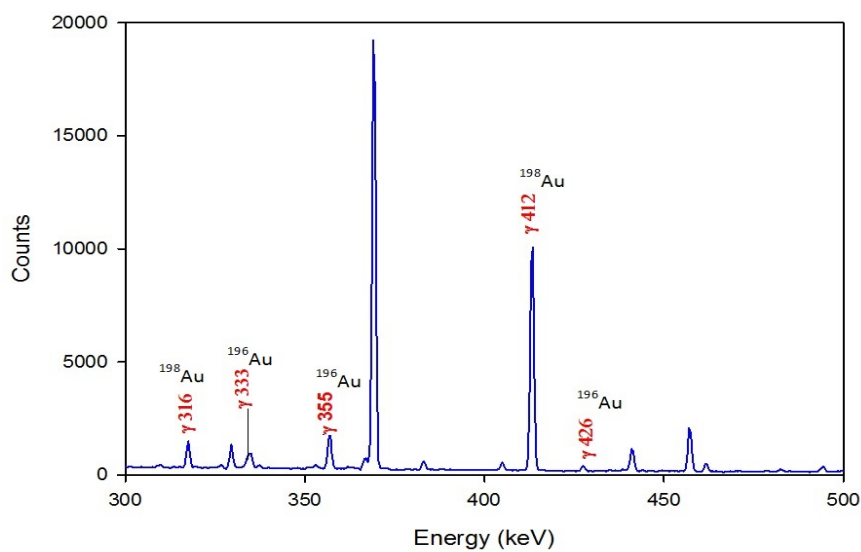
Figure B.4 – Typical γ-ray spectrum of the Blank target after chemical separation zoomed in the region of isomeric decays and ground states for both ^{196}Au and ^{198}Au.
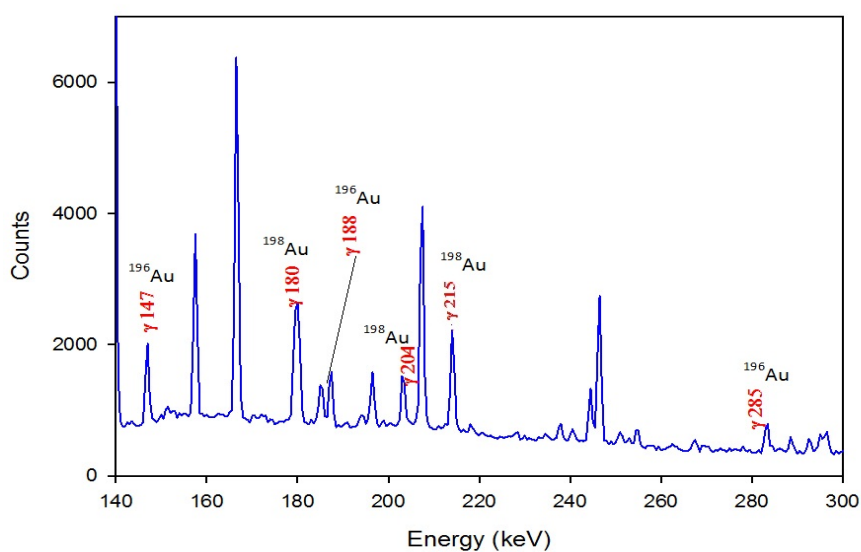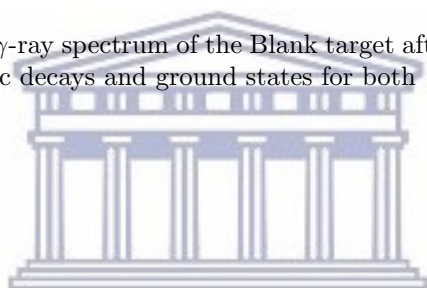
Figure B.5 – Typical γ-ray spectrum of the Far target after chemical separation zoomed in the region of isomeric Screenshot of a for both ^{196}Au and ^{198}Au.
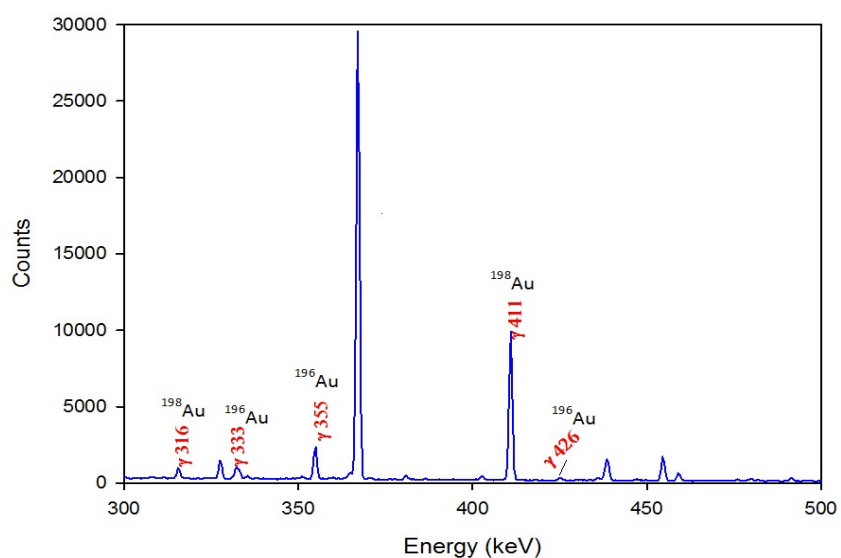
Figure B.6 – Typical γ-ray spectrum of the Far target after chemical separation zoomed in the region of isomeric decays and ground states for both ^{196}Au and ^{198}Au.

Appendix C

C.1

Intensity and efficiency corrected number of counts

Count.(h)	keV	Decays	Decays $_{lower}$	Decays $_{upper}$
12	204	60311	53727	119459
24	204	109844	100679	161240
36	204	149792	138881	16747
48	204	183716	171297	196747
60	204	211195	197727	225324
12	215	56334	51962	60959
24	215	104857	98346	111728
36	215	147923	139744	156556
48	215	184644	175125	194692
60	215	213536	202936	224725
12	412	1220635	1181648	126154
24	412	1163633	1612527	1717252
36	412	1919884	1861871	1980749
48	412	2118134	2054734	2184652
60	412	2295914	2227852	2367323

Table C.1 – ^{198}Au intensity and efficiency corrected counts for the close target.

67

Count.(h)	keV	Decays	Decays $_{lower}$	Decays $_{upper}$
12	204	117700	109840	125997
24	204	224128	211953	236979
36	204	312088	296517	328523
48	204	400345	381659	420067
60	204	466055	445064	488211
12	215	118590	1113126	123527
24	215	253906	2466781	261205
36	215	327427	319665	335350
48	215	402229	393850	410745
60	215	471805	462807	480936
12	412	1168511	1113126	1228805
24	412	1887975	1825949	1953613
36	412	2463986	2399821	2531011
48	412	2966463	2900095	3035318
60	412	3418665	3350500	3489072

Table C.2 – ^{198}Au intensity and efficiency corrected counts for the far target.

Count.(h)	keV	Decays	Decays $_{lower}$	Decays $_{upper}$
12	147	126121	117395	141500
24	147	182246	171655	198426
36	147	196001	186967	209783
48	147	216004	204288	232477
60	147	217502	205571	233974
12	188	207887	183017	252524
24	188	321732	288158	373535
36	188	383655	345549	439316
48	188	437201	396186	495024
60	188	480381	435304	542237
12	355	96847	86007	137731
24	355	191894	176657	234922
36	355	288206	270060	332710
48	355	374728	355107	419478
60	355	458636	435732	506266

Table C.3 – ^{196}Au intensity and efficiency corrected counts for the close target.

Count.(h)	keV	Decays	Decays $_{lower}$	Decays $_{upper}$
12	147	123993	116563	131874
24	147	171309	162336	180740
36	147	177161	167827	186946
48	147	190591	180649	201003
60	147	195249	184632	206357
12	188	180902	158916	191191
24	188	262833	233573	278018
36	188	286236	255742	302826
48	188	300871	268332	319183
60	188	304386	271632	323412
12	355	256922	24712	267183
24	355	498880	486129	511997
36	355	733037	718684	747693
48	355	955238	939709	971023
60	355	1161897	1145271	1178756

Table C.4 – ^{196}Au intensity and efficiency corrected counts for the far target.
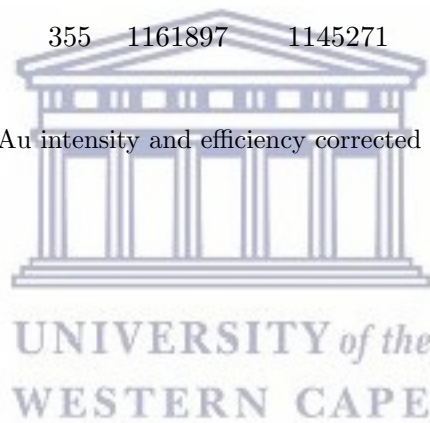
Appendix D

D.1 MATLAB source code

```
1
2   close all
3   clc
4
5   %entering the parameters
6
7   %NduringI, Nn and N are the functions that needs modification. Enter the
8   %halflives in each of these. Also note that a current must be entered, see
        further down in the code.
9   variables;
10
11  Decay1=isomer; % Enter measured decays. 1 is isomer, 2 is ground
12  Decay2=ground;
13  CalcDecay1=0;
14  CalcDecay2=0;
15  N1=Decay1;
16  N2=Decay2;
17  N1tb=0;
18  N2tb=0;
19  N1high=1000*N1;
20  N2high=1000*N2;
21
22  %enter decay constant in /h or /m or /s
23
24  thalf_1=; %halflife of an isomer
25  thalf_2=; %halflife of an ground
26  lambda1=log(2)/thalf_1;
27  lambda2=log(2)/thalf_2;
28
29  %Enter values for times
30
31  tend=;   %Counting time in hours
32  tcount=; % time between the beam shut off and counting began
33  tbeam=;  %Time the beam was active.
34
35  while abs(Decay1-CalcDecay1) > 1
36      [t,y]=RK34(@Nn,N1,tcount,tend);
37      CalcDecay1=(N1-y(1,end));
```

70

```matlab
38        if abs(Decay1-CalcDecay1) > 1
39            if CalcDecay1 > Decay1
40                N1high=N1;
41                N1=N1/2;
42            else
43                N1=N1+(N1high-N1)/2;
44            end
45        end
46
47  end
48
49  [t2,y2]=RK34(@N,[N1;0],tcount,tend);
50  PartDecay2=N1-y2(1,end)-y2(2,end); %Calculates the isomer's contribution to the
        groundstate's decays.
51
52  while abs(Decay2-CalcDecay2) > 1
53      [t4,y4]=RK34(@N,[0;N2],tcount,tend);
54      CalcDecay2=PartDecay2+(N2-y4(2,end));
55      if abs(Decay2-CalcDecay2) > 1
56          if CalcDecay2 > Decay2
57              N2high=N2;
58              N2=N2/2;
59          else
60              N2=N2+(N2high-N2)/2;
61          end
62      end
63      N2;
64  end
65  [tc,yc]=RK34(@N,[N1;N2],tcount,tend);
66
67  N1tb=1000*N1;
68  N2tb=1000*N2;
69  N1tc=0;
70  N2tc=0;
71  N1high=10*N1;
72  N2high=10*N2;
73  while abs(N1-N1tc) > 1
74      [tl,yl]=RK34(@Nn,N1tb,0,tcount);
75      N1tc=yl(1,end);
76      if abs(N1-N1tc) > 1
77
78          if N1tc > N1
79              N1high=N1tb;
80              N1tb=N1tb/2;
81          else
82              N1tb=N1tb+(N1high-N1tb)/2;
83          end
84      end
85  end
86
87  while abs(N2tc-N2) > 1
88      [tk,yk]=RK34(@N,[N1tb;N2tb],0,tcount);
89      N2tc=yk(2,end);
90      if abs(N2tc-N2) > 1
91          if N2tc > N2
```
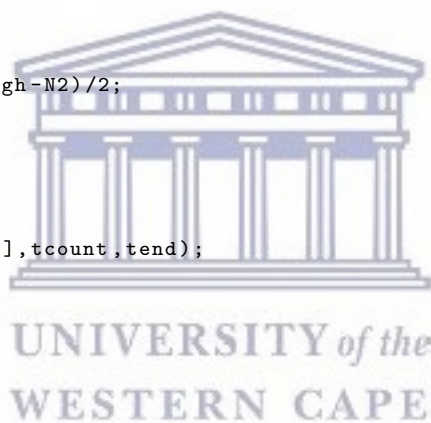
```matlab
 92                  N2high=N2tb;
 93                  N2tb=N2tb/2;
 94              else
 95                  N2tb=N2tb+(N2high-N2tb)/2;
 96              end
 97          end
 98      end
 99
100      [tb,yb]=RK34(@N,[N1tb;N2tb],0,tcount);
101
102      A=N1tb; %Production rates and initial values that are not true (to start the
                iteration).
103      B=N2tb;
104      Ahigh=N1tb;
105      Bhigh=N2tb;
106      CalcN1tb=0;
107      CalcN2tb=0;
108      CalcA=0;
109      CalcB=0;
110      %
111      % Enter the current information as a vector, time step is 1 sec.
112      load .txt ; % .mat .xlsx ect.
113      Current= ;  %  use the loaded Current file
114
115
116      while abs(N1tb-CalcN1tb) > 1
117          [~,yi]=RK342I(@NduringI,[0;0],0,tbeam,A,B,Current);
118          CalcN1tb=yi(1,end);
119          if abs(N1tb-CalcN1tb) > 1
120              if CalcN1tb > N1tb
121                  Ahigh=A;
122                  A=A/2;
123              else
124                  A=A+(Ahigh-A)/2;
125              end
126          end
127      end
128
129      [ti2,yi2]=RK342I(@NduringI,[0;0],0,tbeam,A,0,Current);
130
131      while abs(N2tb-CalcN2tb) > 1
132          [ti3,yi3]=RK342I(@NduringI,[0;0],0,tbeam,A,B,Current);
133          CalcN2tb=yi3(2,end);
134          if abs(N2tb-CalcN2tb) > 1
135              if CalcN2tb > N2tb
136                  Bhigh=B;
137                  B=B/2;
138              else
139                  B=B+(Bhigh-B)/2;
140              end
141          end
142      end
143
144      [ti,yi4]=RK342I(@NduringI,[0;0],0,tbeam,A,B,Current);
145      td=[0,tbeam];
```
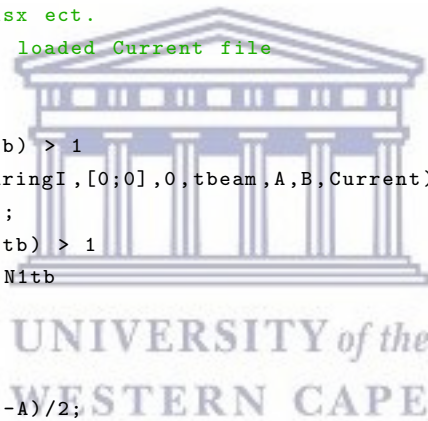
```matlab
146
147  sprintf('%f',A); %print value of A
148  sprintf('%f',B); %print value of B
149
150  % filename='.xlsx'; %spreadshet to store values of A and B for each run
151  values={A,B};
152
153   % xlswrite(filename,values,'sheet1','cell number'); % save A and B the
         spreadsheet created on specific cells
154
155  %%%%%%%%%%%%%%%%%%%%%%%%%%%%%%%%%%%%%%%%%%%%%%%%%%%%%%%%%%%%%%%%%%%%%%%%%%
156          %%%%%%%%%%%%%%%%%%% Plotting %%%%%%%%%%%%%%%%%%%
157  %%%%%%%%%%%%%%%%%%%%%%%%%%%%%%%%%%%%%%%%%%%%%%%%%%%%%%%%%%%%%%%%%%%%%%%%%%
158
159  figure(9)
160  plot(Current) %plot current results
161
162  %ploting the decay equations with the simulated values of A and B
163
164  set(0,'defaulttextinterpreter','none');
165  figure(10)
166
167  hold on
168  % plot(ti,yi4(1,:),'.r');
169  % plot(ti,yi4(2,:),'.b');
170  % plot(tb,yb(1,:),'.r');
171  % plot(tb,yb(2,:),'.b');
172  plot(tc,yc(1,:),'.r'); %green showing the range f
173  plot(tc,yc(2,:),'.b');
174  hold off
175
176  set(gca,'fontsize',18)
177  set(gca,'LineWidth',3);
178  legend('Isomer', 'Ground state');
179  xlabel('Time(min)');
180  ylabel('Population');
181  grid on
182
183  %the end
```

D.2   MATLAB graphs
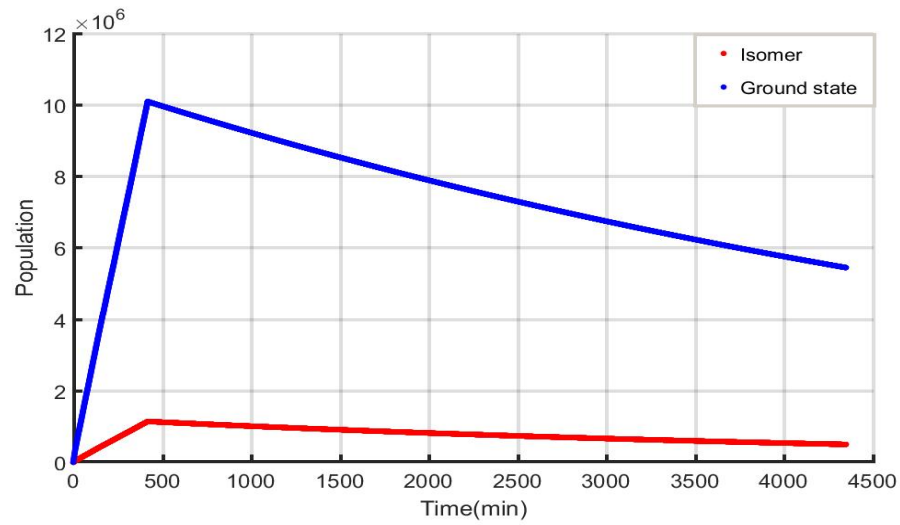
Figure D.1 – Plot of population over time for gold ^{198}Au in the Blank target. The red line is the population of the isomer and the blue line is the population of the ground state.
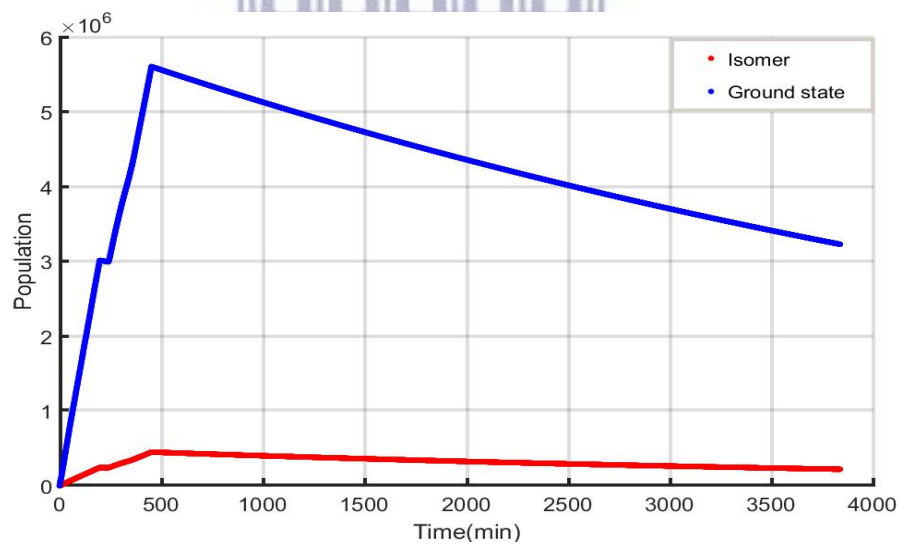
Figure D.2 – Plot of population over time for ^{198}Au in the Close target. The red line is the population of the isomer and the blue line is the population of the ground state. The sudden change in population at 200 - 300 min is when the beam shut off.
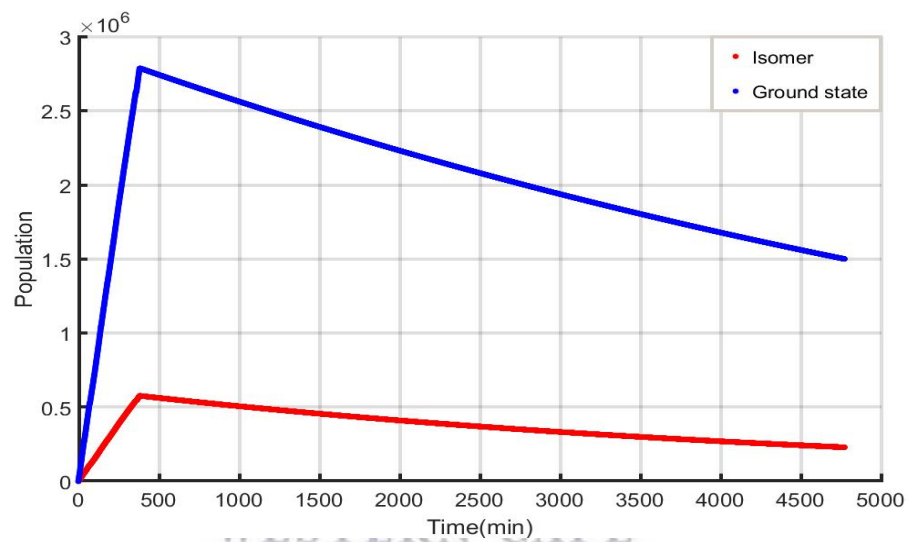
Figure D.3 – Plot of population over time for ^{198}Au in the Far target. The red line is the population of the isomer and the blue line is the population of the ground state.

Appendix E

E.1 Excel Solver spreadsheet

Using the non-linear curve fitting in Excel known as Solver(Microsoft Excel add-in program), the spreadsheet similar to Table E.1below was created. The first two column are containing the time values in minutes and beam current in nA respectively. The third and fourth columns were used to calculate the isomer and ground state population at the given times i.e. $[0, t_{irradiation}]$, $[t_{irradiation}, t_{transport}]$ and $[t_{transport}, t_{counting}]$, where the populations were obtained by using the following equations:

$$N_{iso}(i+1) = N_{iso}(i)[\lambda_{iso}N_{iso}(i) + AI(t(i))]dt \tag{E.1}$$

$$N_{ground}(i+1) = [\lambda_{ground}N_{ground}(i) + \lambda_{iso}N_{iso}(i) + BI(t(i))]dt \tag{E.2}$$

76

Time (min)	Current (nA)	N_{isomer} (t)	N_{ground} (t)	$t_{irradiation}$	420	min
0	0	0	0	$t_{transport}$	1500	min
1	16	748.670	4893.985	$t_{counting}$	3600	min
2	17	1544.028	10090.621	λ_{isomer}	1.375E-4	min^{-1}
3	17	2339.278	15283.836	λ_{ground}	6.795E-4	min^{-1}
4	16	3087.626	20167.757	A	46.791	
5	17	3882.664	25354.336	B	305.874	
6	17	4677.591	30537.500			
7	17	5472.410	35717.250			
8	17	6267.119	40893.590			χ^2
9	17	7061.719	46066.522	D_{excel_isomer}	99999.999	
10	17	7856.210	51236.048	$D_{measured\_isomer}$	100000	10^{-20}
11	17	8650.591	56402.170			
12	17	9444.864	61564.891	D_{excel_ground}	800000.058	10^{-17}
13	17	10239.027	66724.212	$D_{measured\_ground}$	800000	
14	16	10986.288	71574.263			
15	16	11733.448	76421.121			
16	17	12527.296	81570.661			
.	.	.	.			
.	.	.	.			
.	.	.	.			
5520	0	150321.239	91223.964			

Table E.1 – Solving the production rate A and B using Excel Solver, this I testing values i.e. not for Blank, Far or Close target.

Bibliography

[1] Y. Izawa and C. Yamanaka. Production of ^{235}U by nuclear excitation by electron transition in a laser produced uranium plasma. *Physics Letters B*, 88(1): 59 – 61, 1979. ISSN 0370-2693. doi: http://dx.doi.org/10.1016/0370-2693(79) 90113-8. URL http://www.sciencedirect.com/science/article/pii/0370269379901138.

[2] P. Morel, J.M. Daugas, G. Gosselin, V. Méot, and D. Gogny. Nuclear excitation by electronic processes: NEEC and NEET effects. *Nuclear Physics A*, 746:608–612, 2004. ISSN 0375-9474. doi: http://dx.doi.org/10.1016/j.nuclphysa.2004.09.097. URL http://www.sciencedirect.com/science/article/pii/S0375947404010656.

[3] S. Kishimoto, Y. Yoda, M. Seto, Y. Kobayashi, S. Kitao, R. Haruki, T. Kawauchi, K. Fukutani, and T. Okano. Observation of nuclear excitation by electron transition in ^{197}Au with synchrotron x rays and an avalanche photodiode. *Phys. Rev. Lett.*, 85:1831–1834, 2000. doi: 10.1103/PhysRevLett.85. 1831. URL https://link.aps.org/doi/10.1103/PhysRevLett.85.1831.

[4] T. Carreyre, M. R. Harston, M. Aiche, F. Bourgine, J. F. Chemin, G. Claverie, J. P. Goudour, J. N. Scheurer, F. Attallah, G. Bogaert, J. Kiener, A. Lefebvre, J. Durell, W. E. J. P. Grandin, Meyerhof, and W. Phillips. First direct proof of internal conversion between bound states. *Phys. Rev. C*, 62:024311, 2000. doi: 10.1103/PhysRevC.62.024311. URL https://link.aps.org/doi/10.1103/PhysRevC.62.024311.

[5] D. L. Bleuel, L. A. Bernstein, C. A. Brand, W. S. Cassata, B. H. Daub, L. S. Dauffy, B. L. Goldblum, J. M. Hall, C. A. Hagmann, L. B. Hopkins, H. Y. Khater, A. L. Kritcher, D. H. G. Schneider, S. Siem, C. A. Velsko, and M. Wiedeking. Method for detection of nuclear-plasma interactions in a ^{134}Xe-doped exploding pusher at the National Ignition Facility. *Plasma and Fusion Research*, 11:3401075–3401075, 2016. doi: 10.1585/pfr.11.3401075.

[6] P. A. Chodash, J. T. Burke, E. B. Norman, S. C. Wilks, R. J. Casperson, S. E. Fisher, K. S. Holliday, J. R. Jeffries, and M. A. Wakeling. Nuclear excitation by electronic transition of ^{235}U. *Phys. Rev. C*, 93:034610, Mar 2016. doi: 10.1103/PhysRevC.93.034610. URL https://link.aps.org/doi/10.1103/PhysRevC.93.034610.

[7] Ch J Cerjan, L Bernstein, L Berzak Hopkins, R M Bionta, D L Bleuel, J A Caggiano, W S Cassata, C R Brune, J Frenje, M Gatu-Johnson, N Gharibyan, G Grim, Chr Hagmann, A Hamza, R Hatarik, E P Hartouni, E A Henry, H Herrmann, N Izumi, D H Kalantar, H Y Khater, Y Kim, A Kritcher, Yu A Litvinov, F Merrill, K Moody, P Neumayer, A Ratkiewicz, H G Rinderknecht, D Sayre, D Shaughnessy, B Spears, W Stoeffl, R Tommasini, Ch Yeamans, C Velsko, M Wiescher, M Couder, A Zylstra, and D Schneider. Dynamic high energy density plasma environments at the national ignition facility for nuclear science research. *Journal of Physics G: Nuclear and Particle Physics*, 45(3):033003, 2018. URL http://stacks.iop.org/0954-3899/45/i=3/a=033003.

[8] M. Arnould, S. Goriely, and K. Takahashi. The r-process of stellar nucleosynthesis: Astrophysics and nuclear physics achievements and mysteries. *Physics Reports*, 450(46):97–213, 2007. ISSN 0370-1573. doi: http://dx.doi.org/10.1016/j.physrep.2007.06.002. URL http://www.sciencedirect.com/science/article/pii/S0370157307002438.

[9] Z. Y. Bao, H. Beer, F. Käppeler, F. Voss, K. Wisshak, and T. Rauscher. Neutron Cross Sections for Nucleosynthesis Studies. *Atomic Data and Nuclear Data Tables*, 76:70–154, September 2000. doi: 10.1006/adnd.2000.0838.

[10] Ren Reifarth. The s-process overview and selected developments. *Journal of Physics: Conference Series*, 202(1):012022, 2010. URL http://stacks.iop.org/1742-6596/202/i=1/a=012022.

[11] B. V. Kheswa. *Investigation of the 2+ Hoyle state candidates in ^{12}C*. PhD thesis, University of Stellenbosch, 2014.

[12] Adriana Palffy, Zoltan Harman, Christophor Kozhuharov, Carsten Brandau, Christoph H. Keitel, Werner Scheid, and Thomas Stohlker. Nuclear excitation by electron capture followed by fast x-ray emission. *Phys. Lett.*, B661:330–334, 2008. doi: 10.1016/j.physletb.2008.02.027.

[13] C. Granja, J. Kuba, A. Haiduk, and O. Renner. Survey of nuclei for low-energy nuclear excitation in laser-produced plasma. *Nuclear Physics*

A, 784(1):1 – 12, 2007. ISSN 0375-9474. doi: https://doi.org/10.1016/j.nuclphysa.2006.12.003. URL http://www.sciencedirect.com/science/article/pii/S0375947406009742.

[14] G. Gosselin and P. Morel. Enhanced nuclear level decay in hot dense plasmas. *Phys. Rev.*, C70:064603, 2004. doi: 10.1103/PhysRevC.70.064603.

[15] Pálffy, Adriana and Evers, Jörg and Keitel, Christoph H. Isomer Triggering via Nuclear Excitation by Electron Capture. *Phys. Rev. Lett.*, 99:172502, Oct 2007. doi: 10.1103/PhysRevLett.99.172502. URL https://link.aps.org/doi/10.1103/PhysRevLett.99.172502.

[16] V.Meot. *CEA (unpublished)*, 2016. URL http://www-phynu.cea.fr/.

[17] et al. A. L. Kritcher. *(in preparation)*.

[18] S. Kishimoto, Y. Yoda, M. Seto, Y. Kobayashi, S. Kitao, R. Haruki, T. Kawauchi, K. Fukutani, and T. Okano. Observation of nuclear excitation by electron transition in ^{197}Au with synchrotron x rays and an avalanche photodiode. *Phys. Rev. Lett.*, 85:1831–1834, 2000. doi: 10.1103/PhysRevLett.85.1831. URL https://link.aps.org/doi/10.1103/PhysRevLett.85.1831.

[19] S. Kishimoto, Y. Yoda, Y. Kobayashi, S. Kitao, R. Haruki, and M. Seto. Evidence for nuclear excitation by electron transition on ^{193}Ir and its probability. *Nuclear Physics A*, 748(1):3 – 11, 2005. ISSN 0375-9474. doi: https://doi.org/10.1016/j.nuclphysa.2004.10.016. URL http://www.sciencedirect.com/science/article/pii/S0375947404011066.

[20] Irshad Ahmad, R Dunford, Henning Esbensen, D Gemmell, Elliot Kanter, U Rtt, and S H. Southworth. Nuclear excitation by electronic transition in ^{189}Os. 61, 04 2000.

[21] G.F. Knoll. *Radiation Detection and Measurement*. John Wiley, Orlando, 3rd edition, 1999. ISBN 0471073385.

[22] R. D. Evans. *The Atomic Nucleus*. McGraw-Hill Book Co., New York, 1955. ISBN 13: 978-0898744149.

[23] The National Institute of Standards and Technology (NIST), 2017. URL https://physics.nist.gov/PhysRefData/XrayMassCoef/ElemTab/z79.html.

[24] J. L. Glover, C. T. Chantler, Z. Barnea, N. A. Rae, and C. Q. Tran. Measurement of the x-ray mass-attenuation coefficients of gold, derived quantities

between 14 keV and 21 keV and determination of the bond lengths of gold. *Journal of Physics B: Atomic, Molecular and Optical Physics*, 43(8):085001, 2010. URL http://stacks.iop.org/0953-4075/43/i=8/a=085001.

[25] H. Fiedler and O. Tench. Germanium(Li) Gamma Spectrometer Systems. 45 Gracey Avenue, Meriden, Conn. 06450, 1968.

[26] M. Rizzi, M. D'Aloia, and B. Castagnolo. Semiconductor detectors and principles of radiation-matter interaction. *Journal of Applied Sciences (Faisalabad)*, 10(23):3141–3155, 2010.

[27] A. H. F. Muggleton. Semiconductor devices for gamma ray, x ray and nuclear radiation detection. *Journal of Physics E: Scientific Instruments*, 5(5):390, 1972. URL http://stacks.iop.org/0022-3735/5/i=5/a=001.

[28] D. Reilly, N. Ensslin, H. Smith Jr., and S. Kreiner. *Passive Nondestructive Assay of Nuclear Materials*. US Nuclear Regulatory Commission, 1991. ISBN 0160327245.

[29] A. Khaplanov. *Position-sensitive germanium detectors for gamma-ray tracking, imaging and polarimetry*. PhD thesis, A. Khaplanov Royal Institute of Technology (KTH), Stockholm, Sweden, 1993.

[30] T. S. Dinoko. *Search for Low Spin Collective Structures in* ^{158}Er *and* ^{159}Er. PhD thesis, Unversity of the Western Cape, 2013.

[31] Canada and Canadian Nuclear Safety Commission and Commission Canadienne De Sûreté Nucléaire. *Radiation Safety Officers Handbook: Part A*. Canadian Nuclear Safety Commission, 2000. ISBN INFO-0718 ACRP 20 / CCRP 20. URL http://nuclearsafety.gc.ca/pubs_catalogue/uploads/I0718e.pdf.

[32] Pamputt. Atomic rearrangement following an electron capture, 2017. URL https://commons.wikimedia.org.

[33] L. van Dommelen. *Fundamental Quantum Mechanics for Engineers*. Wiley-New York, 2007. URL https://www.eng.fsu.edu/~dommelen/quantum/.

[34] F. F. Karpeshin and M. B. Trzhaskovskaya. Bound internal conversion versus nuclear excitation by electron transition: Revision of the theory of optical pumping of the ^{229m}Th isomer. *Phys. Rev. C*, 95:034310, 2017. doi: 10.1103/PhysRevC.95.034310. URL https://link.aps.org/doi/10.1103/PhysRevC.95.034310.

[35] Masato Morita. Nuclear excitation by electron transition and its application to ^{235}U separation. *Progress of Theoretical Physics*, 49(5):1574, 1973. doi: 10.1143/PTP.49.1574. URL +http://dx.doi.org/10.1143/PTP.49.1574.

[36] S. Kishimoto, Y. Yoda, Y. Kobayashi, S. Kitao, R. Haruki, R. Masuda, and M. Seto. Nuclear excitation by electron transition on ^{197}Au by photoionization around the $K-$absorption edge. *Phys. Rev. C*, 74:031301, 2006. doi: 10.1103/PhysRevC.74.031301. URL https://link.aps.org/doi/10.1103/PhysRevC.74.031301.

[37] K. Hosono, K. Aoki, K. Tanimoto, M. Terasawa, H. Yamaoka, M. Tosaki, Y. Ito, A. Mihai Vlaicu, K. Taniguchi, and T. Jyunichi. Probability of nuclear excitation by electron transition in *Os* atoms. In *APS Meeting Abstracts*, 2001.

[38] M.R. Harston. Analysis of probabilities for nuclear excitation by near-resonant electronic transitions. *Nuclear Physics A*, 690(4):447 – 455, 2001. ISSN 0375-9474. doi: http://dx.doi.org/10.1016/S0375-9474(01)00358-X. URL http://www.sciencedirect.com/science/article/pii/S037594740100358X.

[39] E. V. Tkalya. Theory of the nuclear excitation by electron transition process near the K edge. *Phys. Rev. A*, 75:022509, 2007. doi: 10.1103/PhysRevA.75.022509. URL https://link.aps.org/doi/10.1103/PhysRevA.75.022509.

[40] Yu-kun Ho, Zhu-shu Yuan, Bao-hui Zhang, and Zheng-ying Pan. Self-consistent description for x-ray, Auger electron, and nuclear excitation by electron transition processes. *Phys. Rev. C*, 48:2277–2284, 1993. doi: 10.1103/PhysRevC.48.2277. URL https://link.aps.org/doi/10.1103/PhysRevC.48.2277.

[41] V.I. Goldanskii and V.A. Namiot. On the excitation of isomeric nuclear levels by laser radiation through inverse internal electron conversion. *Physics Letters B*, 62(4):393 – 394, 1976. ISSN 0370-2693. doi: http://dx.doi.org/10.1016/0370-2693(76)90665-1. URL http://www.sciencedirect.com/science/article/pii/0370269376906651.

[42] Adriana Pálffy, Werner Scheid, and Zoltán Harman. Theory of nuclear excitation by electron capture for heavy ions. *Phys. Rev. A*, 73:012715, 2006. doi: 10.1103/PhysRevA.73.012715. URL https://link.aps.org/doi/10.1103/PhysRevA.73.012715.

[43] D. Dauvergne. *General experiments concerning particle-matter interactions; Experiences interdisciplinaires d'interaction particule-matiere.* PhD thesis, Lyon-1 Univ. Claude Bernard, 69 France, 2006.

[44] A. L. Kritcher. Non-LTE Radiation Transport and Nuclear Lifetimes. 2012. URL https://e-reports-ext.llnl.gov/pdf/697232.pdf.

[45] H. A. Bethe. Nuclear Physics B. Nuclear Dynamics, Theoretical. *Rev. Mod. Phys.*, 9:69–244, 1937. doi: 10.1103/RevModPhys.9.69. URL https://link.aps.org/doi/10.1103/RevModPhys.9.69.

[46] H. A. Bethe. An Attempt to Calculate the Number of Energy Levels of a Heavy Nucleus. *Phys. Rev.*, 50:332–341, 1936. doi: 10.1103/PhysRev.50.332.

[47] J. R. Huizenga and R. Vandenbosch. Interpretation of Isomeric Cross-Section Ratios for (n,gamma) and (gamma, n) Reactions. *Phys. Rev.*, 120:1305–1312, 1960. doi: 10.1103/PhysRev.120.1305.

[48] J. B. Wilhelmy, E. Cheifetz, R. C. Jared, S. G. Thompson, H. R. Bowman, and J. O. Rasmussen. Angular momentum of primary products formed in the spontaneous fission of ^{252}Cf. 5:2041–2060, jun 1972. doi: 10.1103/PhysRevC. 5.2041.

[49] W. Hauser and H. Feshbach. The inelastic scattering of neutrons. *Phys. Rev.*, 87:366–373, 1952. doi: 10.1103/PhysRev.87.366. URL https://link.aps.org/doi/10.1103/PhysRev.87.366.

[50] H. Warhanek and R. Vandenbosch. Relative cross-sections for formation of the shielded isomeric pair $^{134m-134}$Cs in medium energy fission. *Journal of Inorganic and Nuclear Chemistry*, 26(5):669 – 676, 1964. ISSN 0022-1902. doi: http://dx.doi.org/10.1016/0022-1902(64)80308-0. URL http://www.sciencedirect.com/science/article/pii/0022190264803080.

[51] J. R. Nix and W. J. Swiatecki. Studies in the liquid-drop theory of nuclear fission. *Nuclear Physics*, 71(1):1 – 94, 1965. ISSN 0029-5582. doi: http://dx.doi.org/10.1016/0029-5582(65)90038-6. URL http://www.sciencedirect.com/science/article/pii/0029558265900386.

[52] D. G. Sarantites, G. E. Gordon, and C. D. Coryell. Ratios of independent yields of the isomers $^{131m-131}$Te and $^{133m-133}$Te in fission. *Phys. Rev.*, 138: B353–B364, 1965. doi: 10.1103/PhysRev.138.B353. URL https://link.aps.org/doi/10.1103/PhysRev.138.B353.

[53] R. Vandenbosch and J. R. Huizenga. Isomeric Cross-Section Ratios for Reactions Producing the Isomeric Pair Hg$^{197-197m}$. *Phys. Rev.*, 120:1313–1318, 1960. doi: 10.1103/PhysRev.120.1313.

[54] D. L. Bleuel. 6th Workshop on Nulear Level Desnity and Gamma Strength. 2017. URL http://tid.uio.no/workshop2017.

[55] L. A. Bernstein. 4th Workshop on Nulear Level Desnity and Gamma Strength. 2013. URL http://tid.uio.no/workshop2013.

[56] A. S. Jensen and J. Sandberg. Analytic nuclear level density formula with shell and pairing effects. *Physica Scripta*, 17(2):107, 1978. URL http://stacks.iop.org/1402-4896/17/i=2/a=009.

[57] C. M. Lyneis, D. J. Clark, and Z. Q. Xie. LBNL 88-Inch Cyclotron Improvements. In *Proceedings, 14th International Conference on Cyclotrons and their Applications (CYCLOTRONS 95), Faure, Cape Town, South Africa, 8-13 Oct 1995*, page E03, 1996. URL http://jacow.org/c95/papers/e-03.pdf.

[58] 10th *International Conference on Cyclotrons and their Applications*, New York, NY, 1984. IEEE, IEEE. URL https://cds.cern.ch/record/106403. Appendix : List of cyclotrons, p. 623-748.

[59] Z. Q. Xie and C. M. Lyneis. Proceedings of the 13th International Workshop on ECR Ion Sources. Texas A&M, College Station, US, 1997.

[60] T. Nakagawa, T. Kurita, M. Kidera, M. Imanaka, Y. Higurashi, M. Tsukada, S. M. Lee, M. Kase, and Y. Yano. Intense beam production from RIKEN 18 GHz ECRIS and liquid He free SC-ECRIS. *Review of Scientific Instruments*, 73(2):513–515, 2002. doi: 10.1063/1.1429314. URL http://dx.doi.org/10.1063/1.1429314.

[61] M. McMahan, D. Leitner, T. Gimpel, J. Morel, B. Ninemire, R. Siero, C. Silver, and R. Thatcher. A 16 MeV/nucleon cocktail for heavy ion testing. *escholarship*, 73:1–4, 2004. URL http://escholarship.org/uc/item/1q9955k5.

[62] R. Gunnick and J. B. Niday. UCRL-51016,LLNL. pages 1–4, 1971-1972.

[63] R. Gunnick and J. B. Niday. Ucrl-53861. pages 1–3, 1988.

[64] B.H. Daub, D. L. Bleuel, M. Wiedeking, L.A. Bernstein, N.M. Brickner, J.A. Brown, B.L. Goldblum, K.S. Holliday, J. Lundgren, and K. Moody. Neutron transfer in the ^{13}C + ^{197}Au reaction from gold isotope residuals. 2016.

[65] T. W. Burrows, C. L. Dunford, and J. K. Tuli. Evaluated And Compiled Nuclear Structure Data:ENSDF Search And Retrieval @online, 2017. URL http://www.nndc.bnl.gov/ensdf/.

[66] D.C. Radford. Notes on the use of the program gf3. http://radware.phy.ornl.gov/gf3/gf3.html, 2016.

[67] San Jose California USA Systat Software, Inc. Statistical software for micro-computers: Sigmaplot 12.0. 2016.

[68] C. A. Bertulani. Theory and Applications of Coulomb Excitation. 2009.

[69] Hyperphysics. Coulomb barrier for nuclear fusion, 18 Oct. 2017. URL http://hyperphysics.phy-astr.gsu.edu/hbase/NucEne/coubar.html.

[70] Private Communication with Darren L. Bleuel (unpublished). 2016.

[71] T. Elliott and M. Spiegelman. 3.14 - melt migration in oceanic crustal production: A u-series perspective. In Heinrich D. Holland and Karl K. Turekian, editors, *Treatise on Geochemistry*, pages 465 – 510. Pergamon, Oxford, 2003. ISBN 978-0-08-043751-4. doi: https://doi.org/10.1016/B0-08-043751-6/03031-0. URL http://www.sciencedirect.com/science/article/pii/B0080437516030310.

[72] X. Giraldo., Francis and M. Restelli. High-order semi-implicit time-integrators for a triangular discontinuous galerkin oceanic shallow water model, 2009. URL https://calhoun.nps.edu/handle/10945/38309.